Physics – Uspekhi **63** (12) 1161 – 1187 (2020)

REVIEWS OF TOPICAL PROBLEMS PACS numbers: **02.70. – c**, **64.30. – t**, 64.70.D –

Does the embedded atom model have predictive power?

D K Belashchenko

DOI: https://doi.org/10.3367/UFNe.2020.01.038761

Contents

Abstract. Potassium, rubidium, aluminum, iron, nickel, and tin embedded atom models (EAMs) have been used as examples to ascertain how well the properties of a metal are described by EAM potentials calculated from the shape of shock adiabats and/or static compression data (from a function of cold pressure). Verification of the EAM potential implies an evaluation of its predictive power and an analysis of the agreement with experiment both at 0 or 298 K and under shock compression. To obtain consistent results, all contributions of collectivized electrons to energy and pressure need to be taken into consideration, especially in transition metals. Taking account of or ignoring electron contributions has little effect on the calculated melting lines of the models, self-diffusion coefficients, and viscosity. The shape of the melting line is sensitive to the behavior of the repulsive branch of the pair contribution to the EAM potential at small distances.

Keywords: embedded atom model (EAM), molecular dynamics method, embedding potential, electron contributions, predictive power, tandem, static compression, shock compression

D K Belashchenko
National University of Science and Technology MISIS,
Leninskii prosp. 4, 119049 Moscow, Russian Federation
E-mail: dkbel75@gmail.com

Received 1 November 2019, revised 19 January 2020
Uspekhi Fizicheskikh Nauk **190** (12) 1233 – 1260 (2020)
Translated by Yu V Morozov

1. Introduction

The era of pair potentials $\varphi(r)$ ended in the main by the end of the 20th century. The concept of pair interaction did not allow simultaneous agreement to be obtained between the calculated properties of a substance and the mechanical and caloric equations of state. The end of the pair potential era closed the door on the further development and application of the theory of simple liquids, which had an almost 60-year history. The time has come for multiparticle potentials. A new promising concept of the embedded atom model (EAM) that emerged in the 1980s paved the way for the use of multiparticle potentials [1–5]. In mathematical terms, the notion of embedding potential was introduced to characterize the energy of an atom in the field of an effective electron charge created by metal atoms. This charge makes possible multiparticle interaction. For the purpose of calculation of interparticle forces, it can be represented as the totality of effective pair interactions with the possibility of molecular dynamics (MD) calculations of metal model properties [6] by enumerating pairs of atoms rather than triplets, as in the action of valence forces.

The majority of studies that have used EAM potentials were aimed at calculating properties of crystalline metals and alloys mainly in limited intervals of the parameters of state — temperature and pressure, usually at absolute zero. Only comparatively new studies are designed to construct metal models in broad temperature and pressure ranges, e.g., under shock compression conditions, when the density increases 1.5–2 times or more and the temperature rises to tens of thousands of degrees.

2. Potential of the embedded atom model

At first, the embedded atom model was intended for MD-modeling of lattice defects, analysis of surface properties, and phase transitions. Numerous EAM potentials published to date have been used to calculate various physicochemical properties of mono- and multicomponent metallic systems. It is impossible to list them all. The embedded atom model is based on the expression for the potential energy of a metal:

$$U_{\text{pot}} = \sum_{i=1}^{N} \Phi(\rho_i) + \sum_{i<j}^{N} \varphi(r_{ij}), \quad \rho_i = \sum_j \psi(r_{ij}), \tag{1}$$

where r_{ij} is the interparticle distance. The first sum is the 'embedding energy' and the second one represents a usual pair interaction with potential $\varphi(r)$. There is no embedding energy in nonmetallic systems. To calculate the total energy, expression (1) needs to be supplemented by the kinetic energy of atoms $(3/2)NkT$ and the thermal energy of the electron gas (if it is taken into consideration). The energy in (1) is calculated with respect to the ideal gas of particles at rest. Function $\psi(r)$ is the effective electron density created by atom j on atom i and the quantity ρ_i is the effective electron density at the point $\mathbf{r}_i$ created by the surrounding atoms. It is convenient to choose the condition $\rho = 1$ in a certain 'standard state' on a crystal atom at $T = 0$ or on an atom of a liquid near the melting point). Functions Φ, φ, and ψ are presented either analytically or in the form of tables.

The embedded atom model can be applied to describe a concrete metal as follows. First, it is necessary to determine the form of the pair contribution $\varphi(r)$ to the EAM potential. For crystalline metals, the problem is solved quantum mechanically. In the case of liquid metals, the function $\varphi(r)$ can also be determined using the diffraction pair correlation function (PCF) of the fluid [7, 8] and the Schommers algorithm [9]. This is the inverse problem of the fluid theory. There are other algorithms for inverse calculation of the pair potential in the form of the PCF using more complex equations of the theory of fluids [10, 11], but there are no particular advantages of their choice, since the inverse problem does not have an unambiguous solution [7, 12]. Other paired contributions to the EAM potential (Lennard-Jones, Morse, etc.) were also used.

As far as the embedding potential is concerned, the form of functions $\Phi(\rho)$ and $\psi(r)$ can be chosen in different ways, e.g., in the form of the Sutton–Chen formulas [5, 13–15]:

$$\Phi(\rho) = -\varepsilon C \rho^{1/2}, \quad \psi(r) = \left(\frac{a}{r}\right)^m,$$
$$\text{with the paired contribution} \quad \varphi(r) = \varepsilon \left(\frac{a}{r}\right)^n, \tag{2}$$

or in the form [16, 17]

$$\Phi(\rho) = -a\left[1 - \ln\left(\frac{\rho}{\rho_e}\right)^n\right]\left(\frac{\rho}{\rho_e}\right)^n + b\left(\frac{\rho}{\rho_e}\right),$$
$$\psi(r) = b \exp\left[-\chi(r - r_e)\right], \tag{3}$$

where a, b, ρ_e, m, and n are parameters, or in the piecewise continuous form, for example [7],

$$\psi(r) = p_1 \exp(-p_2 r),$$

$$\Phi(\rho) = a_1 + c_1(\rho - \rho_0)^2 \quad \text{at} \quad \rho_1 \leqslant \rho \leqslant \rho_6,$$

$$\Phi(\rho) = a_i + b_i(\rho - \rho_{i-1}) + c_i(\rho - \rho_{i-1})^2$$
$$\text{at} \quad \rho_i \leqslant \rho \leqslant \rho_{i-1} (i = 2, 3, 4, 5), \tag{4}$$

$$\Phi(\rho) = [a_6 + b_6(\rho - \rho_1) + c_6(\rho - \rho_1)^2]\left[2\frac{\rho}{\rho_5} - \left(\frac{\rho}{\rho_5}\right)^2\right]$$
$$\text{at} \quad \rho \leqslant \rho_5,$$
$$\Phi(\rho) = a_7 + b_7(\rho - \rho_6) + c_7(\rho - \rho_6)^m$$
$$\text{at} \quad \rho_6 \leqslant \rho \leqslant \rho_7, \tag{5}$$
$$\Phi(\rho) = a_8 + b_8(\rho - \rho_7) + c_8(\rho - \rho_7)^n \quad \text{at} \quad \rho > \rho_7,$$

with $\rho_0 = 1$; at $\rho = \rho_i$, the function $\Phi(r)$ itself and its first derivative are continuous. Additional parts of the function $\Phi(\rho)$ can be added at large ρ. The ρ_i values increase in the following sequence: $\rho_5 < \rho_4 < \rho_3 < \rho_2 < \rho_1 < \rho_0 < \rho_6 < \rho_7$. Finally the EAM potential is determined by the parameters $p_1, p_2, a_1, c_1 - c_8, \rho_1 - \rho_7, m, n$, which allows, in principle, fitting the properties of the models to the experimental data. Expressions (4) and (5) are used to model normal or low-density and high-density states, respectively. Parameters of the expressions for the embedding potential can be found on theoretical grounds as well as from the data of static tests or shock compression experiments. To model a liquid metal, it is convenient to choose the $\psi(r)$ function so that the mean value $\langle\rho\rangle$ of the fluid model near the melting point (in the 'standard state') equals 1. It follows from (4) that in a state with $\rho = \rho_0 = 1$, $\mathrm{d}\Phi/\mathrm{d}\rho \approx 0$, and interparticle forces are determined only by the pair contribution to the potential.

For example, it is convenient to describe the embedding potential $\Phi(\rho)$ by the expression

$$\Phi(\rho) = a_0 + \sum_2^m a_n(\rho - 1)^n. \tag{6}$$

Coefficients a_n can be found from the $p(V)$ dependence at the 298-K isotherm under static compression. Coefficient a_0 is determined from the model energy.

Later authors proposed variants of the EAM potential, such as the modified EAM (MEAM), taking into account the directional coupling [18, 19]. In many cases, EAM potentials are sufficiently accurate to describe a set of properties of the crystalline phase and even to describe several phases of a given metal at a time. However, such high accuracy can be reached only within a limited interval of state parameters, e.g., at absolute zero. The potentials can be insufficiently accurate to describe substances exposed to high temperatures and pressures characteristic of shock compression and astrophysical objects. For example, potentials calculated for Nb and V in [20] lead to the destruction of the crystal lattice at ~ 500 and ~ 1000 K, respectively. Moreover, EAM potentials developed for crystalline substances turn out to be insufficiently accurate for predicting the properties of the liquid or amorphous phase. For this reason, they can not always be used, for example, to calculate the melting line with sufficient accuracy. This poses the question as to whether it is possible to apply EAM potentials in wide ranges of pressures and temperatures. In other words, do EAM potentials have a predictive power? The search for the answer to this question is the central topic of the present review.

It is relatively easy to evaluate the accuracy of EAM potentials to describe metals at moderate temperatures and pressures. For example, the authors of [21] compared the results of calculations of liquid lithium properties (melting lines, vapor pressure, density, structure, and surface tension) obtained with the use of six different EAM potentials at pressures up to ~ 4 GPa and temperatures up to 2200 K. They failed to observe ideal agreement with experiment but managed to distinguish the most accurate potentials.

It is very difficult to describe the temperature dependence of metal properties with the use of embedding potentials, because this dependence becomes apparent only due to a change in effective electron density ρ resulting from thermal expansion or structural modification. An analysis of results of calculations of model properties in fairly wide pressure and temperature ranges is needed to assess the value of embedding potentials. Let's take for an example the Sutton–Chen potential (2). Its parameters for nickel were reported in [13] as $\varepsilon = 0.031774$ eV, $C = 33.5741$, $a = 3.1323$ Å, $n = 8.975$, and $m = 3.631$ with the cutoff radius $r_c = 6.00$ Å (with an additional shift of functions $\varphi(r)$ and $\psi(r)$ to zero at $r = r_c$). Figure 1 presents calculated pressure values for nickel models with potential (2) at the 298-K isotherm in comparison with static compression data [22, 23] and calculated pressure values on the shock adiabat (SA) obtained as described in Section 2.2 below in comparison with the factual data [24–26]. Excellent agreement between theory and experiment was demonstrated for the 298-K isotherm, whereas the calculated pressures in the case of shock compression proved greatly overestimated. This means that the temperature on the calculated adiabat is overestimated, i.e., the heat capacity is underestimated. Indeed, MD calculation usually yields values of model heat capacity C_V close to the classical value $3R$, whereas the heat capacity of real metals can be much higher than that (for example, it is 53.02 J mol^{-1} K^{-1} for chromium at 2000 K and 49.12 J mol^{-1} K^{-1} for uranium at the same temperature). Therefore, a type (2) embedding potential does not ensure agreement with experiment at elevated temperatures without special correction.

We shall consider three main types of states differing in temperature: the metal compression isotherm at 298 K, its shock adiabat (the Hugoniot adiabat), and the metal melting line. Also, the possibility of a simultaneous description of a metal in these states using a single EAM potential will be analyzed. For this purpose, we shall check how accurately the potential found from the shape of the shock adiabat describes pressure on the 298-K isotherm and whether the potential calculated from the form of the cold pressure function is suitable for describing the shock adiabat. In addition, we shall consider the peculiarities of melting line calculation at high pressures.

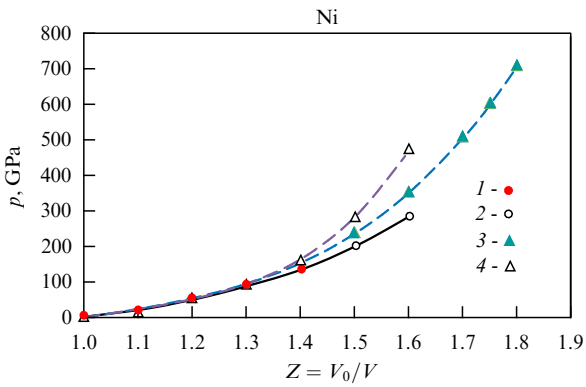

Figure 1. 298-K isotherm and shock adiabat of nickel. *1* — static compression at 298 K [22, 23], *2* — 298-K isotherm with the Sutton–Chen potential (2), *3* — shock adiabat of real nickel [24–26], *4* — calculated shock adiabat with the Sutton–Chen potential. $Z = V_0/V$, where V is the molar volume, V_0 is the standard metal volume.

2.1 Baseline data for the calculation of EAM potential

Experimental data on metal behavior under high pressure are obtained in two main ways: by the methods of static and shock compression. The former usually uses compression of a very small sample in a diamond cell and its heating by a laser beam. The method permits us to reach pressures of millions of atmospheres, but it is rather complicated and has thus far provided data only for a few metals, viz. up to 40 GPa for lithium [27], up to 140 GPa for sodium [28], up to 25 GPa for potassium [29], up to 13 GPa for rubidium [30, 31], up to 5.5 GPa for cesium [31, 32], up to 125 GPa for aluminum [33, 34], up to 100 GPa for lead [31], up to 300 GPa for iron [35], and up to 125 GPa for nickel [36].

The dependence of pressure on the degree of metal compression at 0 or 298 K (the 'cold pressure' function) is often described by the Birch–Murnaghan equation for isothermal substance compression:

$$p(Z) = \frac{3K_0}{2}\left(Z^{7/3} - Z^{5/3}\right)\left\{1 + \frac{3}{4}(K_1 - 4)\left(Z^{2/3} - 1\right)\right\}. \quad (7)$$

Here, $Z = V_{00}/V$, V is the metal volume, V_{00} is the fit parameter, K_0 is the compression modulus, and K_1 is the parameter proportional to the volume derivative of the modulus. Vinet's equation [22] is often used:

$$p(x) = 3K_0(1 - x)x^{-m}\exp\left[1.5(K_1 - n)(1 - x)\right], \quad (8)$$

where $x = (V/V_{00})^{1/3}$, and V_{00}, K_0, K_1, m, n are fit parameters.

There is an extensive shock compression literature, including a comprehensive database that encompasses a wide variety of metals [24]. However, this information is still insufficiently used for calculating interaction potentials.

Figure 1 showing nickel SA [24–26] illustrates the dependence of metal pressure in the region of compression (behind the shock wave front) on the degree of compression $Z = V_0/V$, where V is the molar volume behind the front and V_0 is the standard molar volume. The metal energy E under shock compression is described by the equation [37, 38]

$$E = E_{00} + \frac{1}{2}(p + p_{00})(V_{00} - V), \quad (9)$$

where E_{00}, p_{00}, and V_{00} are the energy, pressure, and volume, respectively, in the initial state. If p_{00} and V_{00} are specified, the shock adiabat is uniquely defined. For example, if the standard state is chosen as the initial state of a metal, then a series of shock tests yields a single principal adiabat. In such a case, the problem of the embedding potential looks like this. Suppose that a calculated potential adequately describes the behavior of the metal (its pressure and energy) along the principal adiabat. Does it correctly describe other states (above or below this adiabat)? Do the properties of the metal obtained based on the shock compression data agree with those deduced from static compression data and vice versa? Is it possible to calculate the melting line in a broad

Table 1. Pressure p on the principal adiabat in the case of SA approximation by polynomials, $Z = V^0_{298}/V$.

Metal	References	Year	Z	p, GPa, for the degree of the polynomial	
				3	4
Sn	[39]	1960	2.00	283.2	284.1
	[25]	1980			
	[40]	1962			
	[26]	1981			
	[25]	1980	2.00	283.5	284.3
	[40]	1962			
	[26]	1981			
	[25]	1980	2.00	286.2	299.7
	[26]	1981			
Fe	[25, 41 – 46]	1957 – 2001	1.70	395.5	395.8
	[7, 24, 25, 43 – 47]	1960 – 2001		398	399.6
	[24, 25, 45 – 47]	1980 – 2001		390.2	390.2
	[24, 45 – 47]	2000 – 2001		392	391.5

pressure range? Finally, does the embedded atom model have a predictive power?

In most recent works on the calculation and application of EAM potentials, either the problem of describing high-temperature states is not posed at all, or the potentials derived from low-temperature data are boldly applied at high temperatures. Obviously, this problem concerns, in particular, the construction of phase diagrams.

The analysis of these issues in the first part of the review is based on the method of considering combinations (tandems) of static and shock compression data. A potential is considered adequate if it accurately describes the properties of a given metal both on the 0-K (or 298-K) isotherm and on the shock adiabat. In the second part of this review, we shall consider possibilities for calculating the melting line of a metal and using experimental data on the melting line to refine the EAM potential.

The use of experimental shock compression data to calculate the potential usually implies the approximation of a large set of pressure values $p(Z)$ on a SA by polynomials. The result of approximation depends on the choice of the source of initial data. Table 1 presents examples of the approximation of tin and iron shock compression data. At a given value of Z, the pressure can change by several GPa and sometimes much more, depending on the literary source, which introduces an uncertainty into the calculation of the potential.

It follows from Table 1 that a natural pressure error of several GPa should be taken into consideration when using shock compression data.

2.2 Relationship between the shape of the shock adiabat and the EAM potential

If the thermal contributions of electrons to the energy and pressure are disregarded, then (for a given pair contribution $\varphi(r)$ in (1)) the embedding potential is determined unambiguously from the SA shape, since the number of thermodynamic degrees of freedom on the SA is equal to unity. When adding

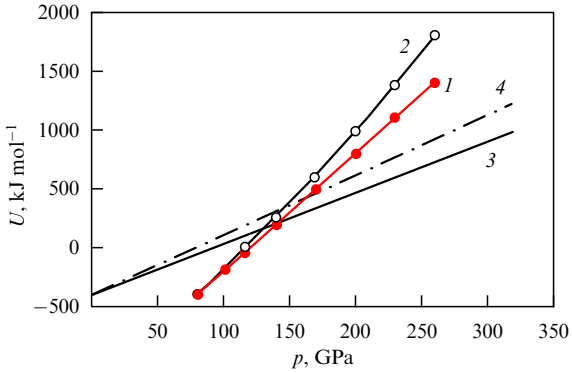

Figure 2. Presentation of the calculation of a point on the shock adiabat at the molar volume V_x. *1* — dependence $E(p)$ for metal models with a given EAM potential, MD method, *2* — the same dependence taking into account the electron contribution to the energy, *3* — graph of equation (9) for a compact metal at $V_{00} = V_0$, where V_0 is the standard molar volume, *4* — graph of equation (9) for an initially porous metal at $V_{00} = mV_0$, where m is the degree of porosity. The intersection points *1–3* and *1–4* determine the states on the shock adiabats of compact and porous metals without taking into account electron contributions; the intersection points of *2–3* and *2–4* are the same, taking into account electron contributions.

the electron contributions, the embedding potential must be changed so that it generates the same initial SA.

To construct the SA of a metal with a known EAM, it is sufficient to calculate the parameters of a series of points lying on the SA. Let us choose a test point with the molar volume of compressed metal V_x and construct by the MD method a series of models with this volume but with different temperatures T_i. For each model, the pressure p_i and the energy $E_i = U_i + (3/2)NkT$ are determined. They define the $E(p)$ dependence for a given volume V_x. If the thermal energy and pressure of electrons are taken into account, they should simply be added to E_i and p_i. Usually, the obtained dependence $E(p)$ is close to a linear one or fairly well approximated by a polynomial of the 2nd or 3rd degree. Its slope at each point is determined by the expression $(\partial E/\partial p)_V = C_V(\partial T/\partial p)_V = V/\gamma$, where $\gamma = (V/C_V)(\partial p/\partial T)_V$ is the Grüneisen coefficient. The coefficient γ is usually on the order of $\sim 0.1 - 1.0$. If the $E(p)$ graph intersects with the graph of equation (9) (the straight line) at $V = V_x$ and $p = p_x$, the intersection point (with pressure p_x and energy E_x) should lie on the SA of the metal with the molar volume V_x. Indeed, the equation of state for the metal and the adiabatic equation (9) at this point are valid. The temperature at this point is simultaneously determined.

This construction is shown in Fig. 2. In what follows, the described method for calculating the adiabat is referred to as the graphical method. Obviously, the same shock adiabat should be obtained with different embedding potentials, depending on the case, whether the electron contributions are taken into account or ignored.

A peculiarity of thermal contributions of the electron gas to the energy and pressure of the metal that appear during heating is that they are usually 'nonpotential', i.e., independent of atom coordinates and determined by metal density and temperature. Models taking no account of electron contributions to the energy and pressure will hereinafter be called parametal models. It is possible to understand how the addition of these thermal contributions (at a constant interparticle potential) affects the SA shape by considering

the pressure dependence of the model energy at a fixed volume in the state on the SA. Figure 2 shows this dependence at $Z = V^0_{298}/V = \text{const}$. Line *1* describes a series of parametal models at $Z = \text{const}$ and different temperatures, and line *3* the SA equation (9) at $Z = \text{const}$. The intersection point of lines *1* and *3* determines the coordinates of the point on the parametal SA. The slope of line *1* is $(\mathrm{d}E/\mathrm{d}p)_V = V/\gamma$, where γ is the Grüneisen coefficient of the parametal model. According to (9), the slope of line *3* is $(\mathrm{d}E/\mathrm{d}p)_V = 0.5(V_{00} - V)$. The inclusion of thermal electron contributions to the energy and pressure yields plot *2* instead of plot *1* (the $E(p)$ dependence). For thermal electron contributions, $(\mathrm{d}E_\mathrm{e}/\mathrm{d}p_\mathrm{e})_V = V/\gamma_\mathrm{e}$, where γ_e is the Grüneisen coefficient of electrons. If $\gamma_\mathrm{e} < \gamma$, the slope of line *2* is greater than that of line *1*, and the intersection point of lines *2* and *3* moves to the left (see Fig. 2). In this case, the pressure and the energy on the SA model with electron contributions decrease in comparison with those in the model ignoring electron contributions. This effect must be roughly proportional to $\gamma - \gamma_\mathrm{e}$.

In the case depicted in Fig. 2, the value of the Grüneisen coefficient of para-potassium near a temperature of 20,000 K is $\gamma = 0.72$. The choice of $\gamma_\mathrm{e} = 2/3$ as in the model of free electrons (MFE) results in $\gamma_\mathrm{e} < \gamma$ and the pressure on the SA of the potassium model, taking into account the electron contributions, being lower than that in the model disregarding them. As γ_e decreases to zero, the effect of pressure reduction on the SA tends toward a maximum.

This line of reasoning leads to the following rule: "If $\gamma > \gamma_\mathrm{e}$, then taking account of thermal electron contributions at the same EAM potential leads to a decrease in the pressure difference along the SA and the 298-K isotherm at the same volume."

2.3 Peculiarities of shock compression of initially porous and liquid specimens

If the initial specimen is in the standard state at 298 K, its molar volume V_{00} is equal to the standard V^0_{298} and the initial energy E_{00} is equal to the standard value E^0_{298}, known from thermodynamic data. If the initial sample is porous, then its initial volume at 298 K $V_{00} = mV^0_{298}$, where m is the degree of porosity. However, the initial energy E_{00} is usually very close to E^0_{298}, since they differ only by a small amount of the metal dispersion energy or the energy of pore formation. Figure 2 shows that the initial porosity increases the pressure and energy at points on the SA. Similarly, it is possible to construct the SA of a metal liquid in the initial state.

2.4 Calculation of the EAM potential from the shape of the shock adiabat

Theoretically, this problem has a unique solution. The choice of the pair contribution to the EAM potential is discussed in Section 2. After choosing the mathematical form of the embedding potential (such as expressions (4) and (5)), one should determine its parameters, taking into account the dependence of the substance density and energy on temperature and pressure both at the 298-K isotherm (the binodal) and on the SA. This stage of calculations is difficult to formalize, and it is usually performed by trial and error (choice of parameters → construction of models by the MD method → comparison with experiment → variation of parameters, etc.). The criterion for the quality of calculations is agreement between the experimental data and the characteristics of the models along both the 298-K/binodal isotherm and the SA.

Reference [7] reports examples of calculations of the EAM potential from shock compression data. The choice of the parametrized form of the EAM potential allows its characteristics to be determined (with or without regard to thermal electron contributions) and metal properties to be calculated under any given conditions. Usually, these parameters are found from the shape of the principal Hugoniot adiabat obtained by compressing the metal from the standard initial state (standard pressure, standard density, temperature 298 K). For each metal there is a single principal Hugoniot adiabat. However, other adiabats can also be obtained by impacting metal samples that are porous in the initial state [38]. Shock compression of porous samples makes it possible to enter the regions of quadrant (p, V) lying above the principal adiabat and to study the metal at much higher temperatures than on the principal adiabat. A wealth of data on shock compression of porous samples was obtained in the second half of the 20th century; sporadic publications on the same topic appeared in the 21st century.

One can get an idea of the accuracy of calculations of the EAM potential from the data on shock compression of porous samples and their agreement with those obtained for compact samples, for example by calculating parameters of the EAM potential from the shape of the principal SA of a compact substance; hereafter, this SA is compared with the "theoretical Hugoniot adiabat"of a porous substance constructed by the aforementioned graphical method. In this case, it is assumed that the substance in the compressed state is in thermodynamic equilibrium.

The described method for finding the theoretical SA of a porous substance (or a substance in any initial state differing from the standard one, e.g., in a liquid state) is suitable for calculations with and without regard to thermal electron contributions. The main thing is that each of these potentials correctly describes $p(V)$ and $E(V)$ dependences on the real SA of a compact substance.

Such calculations were carried out in [7] for copper, cesium, lead, iron, nickel, bismuth, and zinc, taking into consideration electron contributions to the energy and pressure. Let us denote the degree of porosity of the initial sample by $m = V_{00}/V_0$, where V_0 is the initial molar volume of the compact metal in the standard state, and $V_{00} > V_0$ is the actual molar volume of the initial porous metal. By way of example, Fig. 3 shows Hugoniot adiabats of iron at $m = 1.002$, 1.361, and 1.660 [7]. In the cases of copper at $m = 1.00-2.00$, iron at $m = 1.00-1.361$, nickel at $m = 1.108$, and bismuth at $m = 1.486$, the agreement of theoretical and real adiabats is fairly good; at a higher degree of porosity, discrepancies appear that become unacceptably large at $m = 1.66$ for iron, $m = 1.413$ for nickel, and $m = 1.50$ for zinc. We believe that the good agreement between the theoretical and real adiabats testifies in favor of the adequacy of the EAM potential not only along the principal Hugoniot adiabat but also far from it. Consequently, the form of the EAM potential (1) was the correct option in the cases under consideration. The discrepancies at high porosity values appear to be related to peculiarities of the experimental technique. Thus, the results of shock compression of porous samples are hardly worth using for potential calculations.

It should be borne in mind that an analysis of data on shock compression of porous samples does not provide new information on the properties of a substance; it only extends the attainable range of state parameters (pressure, tempera-

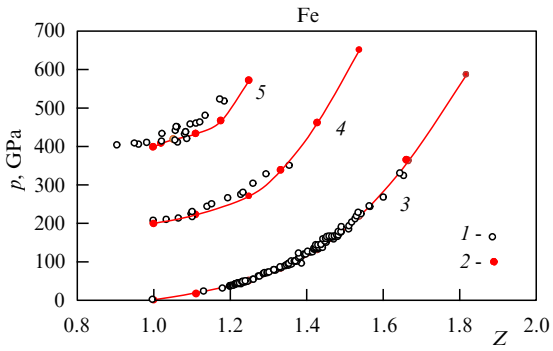

Figure 3. Shock adiabats of iron. *1* — real adiabats [25], *2* — theoretical adiabats [7], *3* — $m = 1.002$, *4* — $m = 1.361$, *5* — $m = 1.660$. Curves *4* and *5* are shifted upward by 200 and 400 GPa, respectively.

ture), mainly in the direction of higher temperatures but lower densities, when the state of the substance approaches that of an ideal gas. Extreme pressure testing (e.g., in underground nuclear explosions [48, 49]) allows the Hugoniot adiabats to be shifted to the region of high densities and temperatures. When constructing MD models with temperatures of millions of degrees, the simple Verlet algorithm may not ensure sufficient accuracy of calculations of model properties; in such cases, higher order algorithms are needed.

Since the temperature on the SA is usually unknown, these data may not provide complete information about the equation of state. Therefore, the properties associated with temperature, heat capacity, etc. remain unknown. To calculate them, certain assumptions about the equation of state of the metal are needed. Progress in shock compression technologies based on the use of high-power laser radiation should be expected in the near future.

2.5 Phenomenological method for the treatment of shock data

The classical molecular dynamics method faces difficulties related to the caloric equation of state, namely, the behavior of heat capacity. Typically, the heat capacity C_V of MD models described by classical mechanics is close to $3R \approx 25$ J mol^{-1} K^{-1} at a variety of potentials. However, the heat capacity of real metals depends on temperature and may differ several-fold from the classical value (see Section 2.1). This difficulty can be overcome by ascribing the discrepancy between theory and experiment to the excitation of the electronic subsystem that contributes to the energy and pressure but does not affect interparticle forces.

A large amount of data on the high-temperature behavior of metals is provided by shock compression experiments. Most of them were carried out before the 1980s, i.e., before the development of the embedded atom model, when calculations of properties at high pressures using interparticle potentials were rare. The then accepted method (standard) for the treatment of shock compression data is described, for example, in [38, 47, 50]. The energy and pressure of the metal are written in the form

$$E(V,T) = E_x(V) + E_T + E_e\,,$$
$$p(V,T) = p_x(V) + p_T + p_e\,, \qquad (10)$$

where $E_x(V)$ and $p_x(V)$ are 'cold' energy and pressure at $T = 0$ (or similar values at 298 K), E_T and p_T are heat additions from crystal lattice vibrations, and E_e and p_e are electron contributions. It is further assumed that

$$E_T = 3R(T - 298)\,, \quad E_e = \frac{1}{2}\beta T^2 \left(\frac{V}{V_0}\right)^m\,,$$
$$p_T = \gamma\frac{E_T}{V}\,, \quad p_e = \gamma_e\frac{E_e}{V}\,. \qquad (11)$$

Here, $C_V = 3R$, $R = 8.314$ J mol^{-1} K^{-1}, $m = 0.5-0.67$ is the electronic heat capacity coefficient derived from low-temperature heat capacity measurements, and the Grüneisen coefficient γ of the substance assumed to depend on the volume alone can be estimated, for example, using the formula [51, 52]

$$\gamma(V) = -\frac{2}{3} - \frac{V}{2}\frac{\mathrm{d}^2 p_x/\mathrm{d}V^2}{\mathrm{d}p_x/\mathrm{d}V}\,. \qquad (12)$$

The introduction of the degree of metal compression $Z = V_0/V$, where V_0 is the standard volume, transforms (12) into

$$\gamma(Z) = \frac{1}{3} + \frac{Z}{2}\frac{\mathrm{d}^2 p_x/\mathrm{d}Z^2}{\mathrm{d}p_x/\mathrm{d}Z}\,. \qquad (13)$$

If the pressure in a certain density range can be approximated by the dependence $p = aZ^q$, it follows from (13) that $\gamma = 1/3 + (q-1)/2$. As for the electron contributions, $\gamma_e = 2/3$ in the free electron model as in an ideal gas. Cold pressure $p_x(V)$ in this calculation scheme is determined experimentally. Of course, the above assumptions of the constancy of heat capacity $C_V = 3R$ and the independence of the Grüneisen coefficient γ of temperature impose limitations on the accuracy of this method.

3. Thermal electron contributions to energy and pressure

In what follows, it will be shown that in many cases nonpotential (thermal) contributions to the energy and pressure coming, for instance, from the presence of free electrons play an important role. In the computer modeling of crystalline metals and alloys, these contributions are now rather rarely taken into account, since they are small at ordinary temperatures. Moreover, the *ab initio* method does not require the separation of electron contributions to the energy and pressure. Nevertheless, constructing MD models at elevated temperatures and pressures is impossible without taking into account the thermal properties of electrons. At the same time, the inclusion of electron contributions into the calculation scheme encounters serious difficulties. Statistical mechanics makes no use of potentials, the parameters of which explicitly depend on temperature or any quantities that can not be expressed directly through the atoms' coordinates. Moreover, the above formulas (11) for E_e and p_e may be far from reality. Therefore, it is important to consider what may be the consequences of ignoring or incorrectly considering thermal electron contributions to the energy and pressure.

3.1 Thermal electron contributions to energy

The problem of considering electron contributions in the context of the application of the molecular dynamics method is not given due attention in the literature. The contribution of electrons to the heat capacity of iron in Earth's core was estimated as amounting to $(1.6-1.8)R$ [53–55]. Calculations

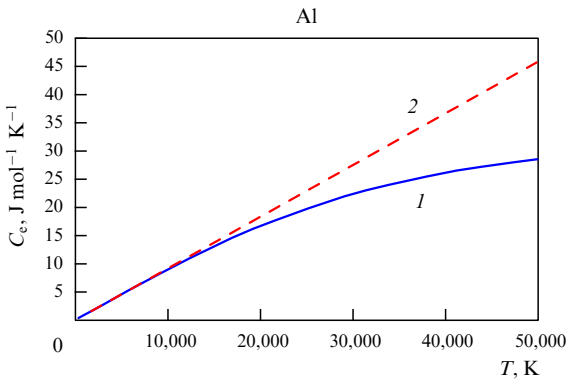

Figure 4. Heat capacity of Al electrons for standard volume $V_0 = 9.993$ cm^3 mol^{-1}. Three collectivized electrons per atom. *1* — equations (14), *2* — Sommerfeld's approximation $C_e = aT$.

of electronic state density and heat capacity at temperatures up to 50,000 K are reported for a group of transition metals (Au, Ni, Cu, Pt, Ag, Al, W, Mo, Ti, Fe) and alloys (Fe–Ni, Cr–Ni) in [56–59]. These data were used in studies by the author of this review to model iron and nickel by the MD method [60]. However, most studies, including MD calculations of melting lines at high pressures, disregard electron contributions.

Simulation of nontransition metals is possible with the use of the free electron model. In this case, two limiting variants of taking the electron contributions into account are available. If valence electrons are completely delocalized, their energy E_e can be calculated in the framework of the MFE using formulas from statistical mechanics [61]:

$$N_e = C\int_0^\infty \frac{\varepsilon^{1/2}\,d\varepsilon}{1+\exp\left((\varepsilon-\mu)/kT\right)}\,,$$
$$E_e = C\int_0^\infty \frac{\varepsilon^{3/2}\,d\varepsilon}{1+\exp\left((\varepsilon-\mu)/kT\right)}\,. \qquad (14)$$

In equations (14), N_e is the number of electrons and μ is their chemical potential. In the MFE, the coefficient $C = 4\pi(2m)^{3/2}V/h^3$, where m is the electron mass, V is the metal volume, and h is the Planck constant. These equations are usually well satisfied for simple liquid metals having an isotropic structure. If N_e, volume V, and temperature T are given, μ can be found from the first equation and E_e from the second one. At low temperatures, Eqns (14) yield the known Sommerfeld solution. Usually, the increment $E_{eT}(T) = E_e(T) - E_e$ (298 K) that vanishes at $T = 298$ K rather than the E_e itself is used. Figure 4 presents the plots of the dependence of electron heat capacity in Al calculated using expressions (14) and the Sommerfeld formula for the heat capacity of an electron gas $C_{eT} = \beta T$. The results of these calculations are in excellent agreement at low temperatures, but the linear dependence markedly overestimates the heat capacity at $T > 10{,}000$ K.

3.2 Thermal electron contributions to pressure

Besides thermal contributions of electrons to the energy, their contribution to the pressure may play an important role. Electron pressure p_{eT} is usually calculated from the equation $p_{eT}V = \gamma_e E_{eT}$ (V is the volume of the metal). The behavior of the electronic Grüneisen coefficient γ_e has been discussed many times in the literature. In the free electron model, $\gamma_e = 2/3$ [61]. In the case of real metals, the value of the electronic Grüneisen coefficient γ_e can be calculated quantum mechanically. For noninteracting electrons, $0 < \gamma_e < 2/3$. Cases of a more complex electron behavior are reported in Ref. [62]. Calculations of electron pressure for Al, Au, Cu, K, Ni, Ta, Ti, and W were carried out, for example, in [59, 63, 64], e.g., for the case of ultrafast laser heating of a metal. A suitable parameterization of these data is required for use in MD modeling. The two simplest cases are considered below. In the first one, electrons behave in accordance with the MFE. In the second case, the valence electrons are thermally excited, but the electron gas is highly localized. For this reason, the thermally excited electrons do not contribute to the pressure and $\gamma_e = 0$. This variant is considered for uranium in [7].

When using results of shock compression to select the EAM potential, the pressure and energy of the electron gas must first be subtracted from the experimental data. After building a metal model, these pressures and energies must again be added to the model properties. Taking into account electron contributions leads to an increase in the heat capacity of the models. As a result, the calculated temperature on the adiabat lowers and the thermal pressure decreases accordingly. At a certain (V_x-dependent) total pressure on the adiabat, the pressure due to interparticle forces increases. Therefore, the pressure at the 298-K isotherm should also increase. However, if the SA is calculated using the potential found from the shape of the 298-K pressure isotherm, taking account of thermal electron contributions leads to a decrease in the calculated pressure on the SA. This inference can be formulated as follows: "when electron thermal corrections are considered, the difference Δp between calculated pressures on SA and at the 298-K isotherm decreases."

To conclude this section, it should be noted that the real interparticle potential may depend on temperature. The simplest example is silicon-like substances in which melting alters the type of bonding. Therefore, the same interparticle potential can not simultaneously describe the behavior of crystalline and liquid phases. Another example is ordinary metals in which the electronic structure changes in response to high-temperature heating. A measure of such changes can be the behavior of the number of delocalized electrons that can be analyzed by quantum mechanical methods. In the case of a simple metal, e.g., aluminum, the number of delocalized (free) electrons remains equal to 3 even during heating to 10^5 K. However, it increases from 2.4 at 0 K to 4.25 at 10^5 K in the case of gold, and from 1.4 at 0 K to 2.9 at 10^5 K in the case of nickel [59]. Evidently, this reduces the number of localized electrons determining the effective ion size; the intreparticle potential must change accordingly. In the considered algorithms for shock data processing, these changes are regarded as thermal electron contributions at variance with their real nature. These effects should naturally manifest themselves in modeling by the *ab initio* method.

Difficulties complicating the use of potentials that depend explicitly on density/temperature are discussed, for example, in Ref. [65].

3.3 Calculation of the EAM potential from static compression data

It was mentioned in Section 2 that pressure dependences of the degree of compression at ~ 298 K had been calculated for certain metals. Such experiments are carried out in diamond cells with the use of laser and/or synchrotron radiation [27–36]. Usually, the parameters of EAM potentials are determined by means of selection, and the criterion for the results is

Table 2. Comparison of the data obtained by EAM and *ab initio* methods.

Metal	d, g cm^{-3}	T, K	N		Number of steps		p, GPa		$D \times 10^5$, cm^2 s^{-1}	
			EAM	*Ab initio*	EAM	*Ab initio*	EAM	*Ab initio*	EAM	*Ab initio*
Ni	13.655	4450	2048	473	5000	59	281.0	332.0	6.02	5.50
Na	2.689	4000	2000	432	5000	1148	70.0	43.9	75.0	64.8
Fe	12.961	6000	2000	432	5000	26	300.0	341.5	6.30	10.9
Bi	17.885	10,000	2000	432	5000	109	100.7	146.0	12.8	11.9

Note. d — density, N — number of model atoms, D — self-diffusion coefficient (B R Gelchinski data).

the proximity of the calculated pressures to those obtained experimentally.

3.4 Use of *ab initio* data for the choice of the EAM potential

Another way to select the EAM potential is quantum mechanical calculations using the Hellmann–Feynman theorem and software tools like Potfit [66]. A set of noncrystalline models of a given metal (built up with any potential) is created, interparticle forces are calculated quantum mechanically, and the form of the EAM potential that could fairly well approximate these forces is selected. In this case, it is very useful to include the liquid phase in the set of test models [67, 68]; then, the EAM potential proves just as well suitable for a fluid. There are few studies of this type, and the accuracy of the described method remains to be thoroughly analyzed.

This method has limitations. *Ab initio* calculations of the metal energy are not sufficiently accurate, because energy variations at the chemical level (~ 1 eV per atom) are some orders of magnitude smaller than in the case of an atom 'undressed' to the state of a 'naked' ion (in the all-electronic version of the calculation) or to pre-valence shells. For example, when the six outer electrons of the iron atom are taken into account in the *ab initio* procedure, the sum of the energies of ionization to the Fe^{+6} state is $\Delta E = 284.33$ eV per atom. Thus, the iron sublimation heat of 4.30 eV per atom is only 1.5% of the ionization energy ΔE. The error of energy calculations by the *ab initio* method is usually $(5-10)\times 10^{-3}$ eV per atom [69]. Calculations of heat capacity on the 100-K basis gives an error on the order of 50–100 J mol^{-1} K^{-1}, considered to be unacceptably large.

It seems that a higher accuracy is possible to achieve when using the *ab initio* method by calculating the diffusion coefficient, pair correlation function, and pressure. Table 2 presents data for four metals undergoing shock compression. The SIESTA package was employed in *ab initio* calculations. The discrepancy between pressure values with respect to EAM data was 15–50% and about the same between self-diffusion coefficients. A better agreement between the results obtained using the EAM method and in experiment was reached by using more accurate *ab initio* programs, such as VASP. For example, the generalized gradient approximation in the theory of the density functional allows discrepancies on the order of 10–15 GPa to be obtained between calculated and measured pressures for iron and nickel [23]. However, even such a discrepancy is too large to regard the calculated data as a reference when fitting the EAM potential.

4. Analysis of data consistency for 298-K isotherm-shock adiabat tandems

When analyzing the adequacy of a potential, it is very informative to compare the equations of state calculated from experimental static and shock data obtained in wide ranges of temperature and pressure. If these data are assumed to be sufficiently accurate (otherwise, they would be unworthy of discussion), the calculated EAM potential should demonstrate their good consistency. A set of static and shock data for a concrete metal will be called a tandem.

Let us consider this problem with reference to potassium, rubidium, aluminum, iron, nickel, and tin tandems. Potassium and rubidium are alkali metals with high compressibility, aluminum is a simple nontransition metal, iron and nickel are transition metals, and tin is a popular subject of the theory of liquids. In the cases of K, Rb, and Al, the MFE can be used (even if with reservations), but it is inapplicable in the case of iron and nickel. For brevity, the models taking no account of electron contributions are called parametal models (para-aluminum, etc.). At the same time, we shall consider how the properties of the models change when the EAM embedding potential is totally ignored, this will permit comparing the roles of the embedding potential $\Phi(\rho)$ and the pair contribution $\varphi(r)$ to the EAM potential. Models totally disregarding the embedding potential (i.e., taking account of the pair contribution $\varphi(r)$ alone) will be called protometal models.

4.1 Potassium tandem

The pair contribution to the EAM potential of potassium was calculated in [70] according to the Schommers algorithm [9] from the form of the pair correlation function (PCF) of liquid potassium near the melting point (T_m). It is shown in Fig. 5. The PCFs of liquid potassium calculated with this potential near T_m practically coincide with the diffraction PCFs [71] (Fig. 6).

Experimental static and shock compression data are currently available for potassium. Shock compression of potassium was investigated in [24, 25, 72]; the potassium SA is shown in Fig. 7. These data were used to calculate the EAM potential of potassium, taking into account the thermal

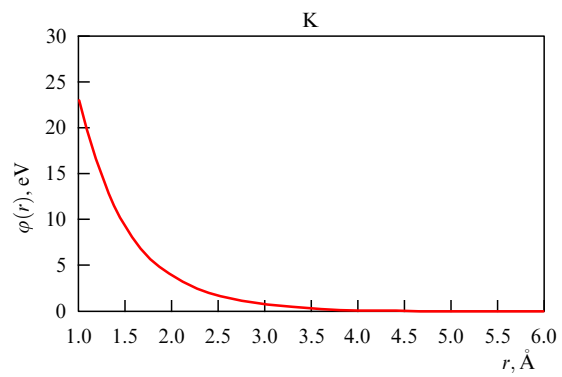

Figure 5. Pair contribution to the potassium EAM potential [70].

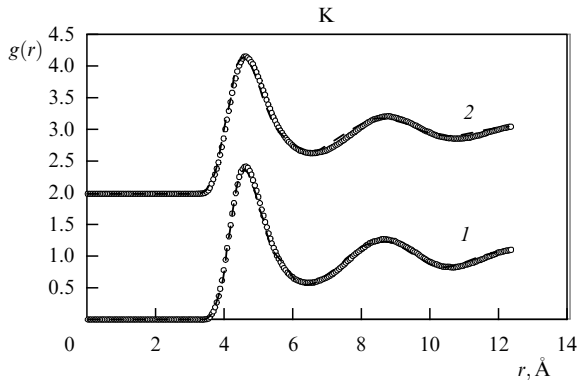

Figure 6. Pair correlation functions of potassium under normal pressure. *1* — 343 K, *2* — 473 K. Dashed lines — diffraction data [71], markers — MD method.

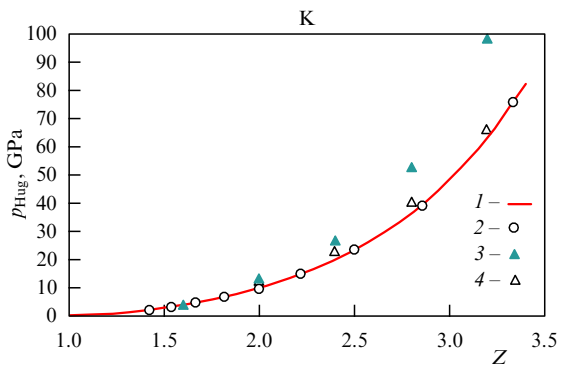

Figure 7. Shock adiabats of potassium. *1* — experiment [25, 72], *2* — EAM-1 potential [7, 73], *3* — EAM-2 potential and $\gamma_e = 2/3$, *4* — EAM-2 potential and $\gamma_e = 0$.

contributions of electrons to the energy and pressure in accordance with the MFE. This potential, shown in Fig. 8, is called the EAM-1 potential. The EAM-1 embedding potential of potassium [7, 73] very well describes the SA (see Fig. 7). The mean-square deviation (MSD) of the calculated pressure from the actual one (columns 4 and 2 of Table 3) is only 0.31 GPa.

The compressibility of potassium at 298 K was also studied by the shock compression method in diamond cells

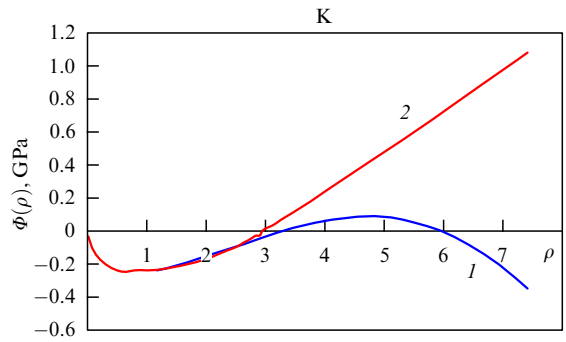

Figure 8. Potassium embedding potentials. *1* — in EAM-1 [7], *2* — in EAM-2.

in the range of 29–51 GPa [75]. The data obtained are described by equation (8) at the following parameter values: $V_{00} = 36.614$ cm^3 mol^{-1}, $K_0 = 8.8$ GPa, $K_1 = 3.1$, $m = 5$, $n = 3$. They are presented in column 5 of Table 3. The 6th column shows the pressures of potassium models with the EAM-1 potential at 298 K. Column 7 shows potassium cold pressures at 298 K calculated from shock compression data using the standard method (see Section 2.5) without taking into consideration thermal electron contributions [72].

It follows from Table 3 that the calculation of the EAM-1 potential underestimates cold pressure in comparison with the static data in the case of modeling by both the MD method with the EAM-1 potential and the standard method without accounting for thermal electron contributions (see Section 2.5). Discrepancies between the pressure values amount to ~ 15 GPa, while the MSD between the numbers in columns 5 and 6 is 7.03 GPa. At a pressure above 10 GPa, the discrepancies may be partly due to the difference between the model (body-centered cubic, bcc) and real (bcc or body-centered tetragonal, bct) potassium structures [76]. However, the pressure of the models weakly depends on the structure. For example, the pressure of the bcc potassium model at 298 K and $Z = 2.50$ is 15.49 GPa and that of the face-centered cubic (fcc) one of equal density is 15.86 GPa. Therefore, it would be possible to improve the agreement with the cold pressure experiment by changing the approach to taking into consideration electron contributions. Cancellation of such consideration in the case of the EAM-1 potential will lead to an additional decrease in cold

Table 3. Properties of bcc potassium models. EAM-1 potential. $V_0 = 45.46$ cm^3 mol^{-1} [74].

$Z = V_0/V$	Shock compression			Cold pressure p_{298}, GPa		
	Experiment p_{Hug}, GPa [25, 72]	EAM-1 [7, 73]		Experiment [75]	EAM-1	Standard method [72]
		T_{Hug}, K	p_{Hug}, GPa			
1	2	3	4	5	6	7
1.6	4.1	826	3.9	3.30	3.07	3.75
1.8	6.7	1448	6.6	5.81	4.86	5.76
2.0	10.0	2601	10.0	8.78	7.44	8.14
2.2	14.2	4478	14.4	12.2	10.60	10.89
2.4	19.9	7273	20.0	16.1	13.78	14.01
2.6	27.3	11,180	27.2	20.4	16.58	17.5
2.8	36.8	16,393	36.5	25.2	19.20	21.4
3.0	48.9	23,106	48.4	30.4	21.81	25.6
3.2	63.8	31,511	63.6	36.0	24.47	30.1
3.4	82.1	41,804	82.8	42.1	27.07	35.0

Note. p_{Hug} — pressure on SA, T_{Hug} — temperature on the adiabat, p_{298} — pressure at 298 K.

pressure and an increase in the discrepancy with the static compression data.

Let us use static compression data as a basis. The EAM embedding potential was calculated from the potassium static compression data [75] in Ref. [70]. Here, it is additionally corrected, and its optimal parameters refined as follows: $\rho_6 = 1.15$, $\rho_7 = 2.90$, $c_7 = 0.052$, $c_8 = 0.012$, $m = 2.00$, $n = 1.50$, in addition to the remaining parameters cited in [7]. We call this potential EAM-2. The data in Table 4 indicate that it very well describes the real potassium pressure isotherm at 298 K (columns 2 and 3), with the MSD between them equaling 0.35 GPa. Also, the embedding potential of potassium for EAM-2 is presented in Fig. 8.

Let us calculate potassium SA using the EAM-2 potential and the aforementioned graphical method both taking into account electron contributions and not doing so. The results of the calculation disregarding electron contributions, i.e., for para-potassium, are presented in Table 4. The calculated pressure values p_{Hug} of para-potassium (column 6) are greatly overestimated compared with the real ones (column 4). The same is true of calculated temperatures. This means that the EAM-2 potential can not be used for SA calculations without proper correction, taking into account electron contributions.

The second variant of calculation envisages consideration of thermal electron contributions. Let us assume that the contribution to the energy is described by the MFE, i.e., by Eqns (14). The graphical method allows such a consideration by adding the electron energy and pressure to the values obtained while constructing the model. Table 4 presents the results of calculations at two values of the electronic Grüneisen coefficient: $\gamma_{\mathrm{e}} = 2/3$ (as in the MFE) and $\gamma_{\mathrm{e}} = 0$ (i.e., ignoring electron contributions to the pressure). The pressure on the SA of para-potassium models is always higher than on the real potassium SA. A transition from para-potassium to the variant with $\gamma_{\mathrm{e}} = 2/3$ results in a reduction in the SA pressure; it further decreases in the variant with $\gamma_{\mathrm{e}} = 0$ (columns 6, 8, and 12 in Table 4). SAs obtained with different interparticle potentials are compared in Fig. 7. The latter variant is regarded as the most suitable (MSD = 1.96).

To sum up, if the experimental data on static and shock compression are accurate and the form of the EAM potential is perfectly adequate, the best results of modeling the potassium tandem are obtained by taking into account the thermal electron contribution to the energy according to the MFE and disregarding the thermal contribution of electrons to the pressure (i.e., $\gamma_{\mathrm{e}} = 0$).

Let us estimate the degree of agreement between the experimental data on static and shock compression of potassium. It should be borne in mind that the experimental static data were obtained up to a pressure of 42 GPa, and the shock data up to 82 GPa. The EAM-1 potential reproduces the real SA with MSD pressure $D_{\mathrm{Hug}} = 0.31$ GPa. The EAM-2 potential reproduces the 298-K isotherm with $D_{\mathrm{cold}} = 0.35$ GPa. Small D_{Hug} and D_{cold} values characterize the quality of fitting EAM potentials according to experimental data. However, the MSD of the calculated cold pressure with EAM-1 (see Table 3) from the actual pressure at the 298-K isotherm $\Delta_{\mathrm{cold}} = 7.03$ GPa. Accordingly, $\Delta_{\mathrm{Hug}} = 1.96$ at $\gamma_{\mathrm{e}} = 0$ and 8.74 at $\gamma_{\mathrm{e}} = 2/3$. High Δ_{cold} and Δ_{Hug} values at $\gamma_{\mathrm{e}} = 2/3$ characterize the deviation of potassium model properties from those of real potassium. The small value of Δ_{Hug} at $\gamma_{\mathrm{e}} = 0$ evidences the agreement between experimental data and the acceptable adequacy of the EAM-2 form at $\gamma_{\mathrm{e}} = 0$. To recall, $\Delta_{\mathrm{cold}} \approx \Delta_{\mathrm{Hug}}$ at $\gamma_{\mathrm{e}} = 2/3$. Table 5 compares the proper-

Table 4. Properties of bcc potassium models at 298 K and on SA. EAM-2 potential. $V_0 = 45.46$ cm^3 mol^{-1}, p_{eT} and E_{eT} — electron contributions.

Z	p_{298}, GPa		SA, EAM-2 potential								
			Experiment p_{Hug}, GPa [25, 72]	Para-potassium		$\gamma_{\mathrm{e}} = 2/3$				$\gamma_{\mathrm{e}} = 0$	
	Experiment [75]	EAM-2		T_{Hug}, K	p_{Hug}, GPa	T_{Hug}, K	p_{Hug}, GPa	p_{eT}, GPa	E_{eT}, kJ mol^{-1}	T_{Hug}, K	p_{Hug}, GPa
1	2	3	4	5	6	7	8	9	10	11	12
1.6	3.30	3.18	4.1	909	4.19	891	4.18	0.01	0.55	886	4.17
1.8	5.81	5.42	6.7	—	—	—	—	—	—	—	—
2.0	8.78	8.71	10.0	4090	12.2	3769	12.1	0.22	7.66	4090	11.81
2.2	12.2	12.5	14.2	—	—	—	—	—	—	—	—
2.4	16.1	16.8	19.9	12,880	26.4	12,189	26.1	1.58	44.91	8829	23.52
2.6	20.4	20.9	27.3	25,690	40.4	—	—	—	—	—	—
2.8	25.2	25.2	36.8	36,945	54.6	24,490	53.0	7.20	175.4	17,658	40.9
3.0	30.4	30.1	48.9	> 45,000	?	—	—	—	—	—	—
3.2	36.0	35.8	63.8	> 90,000	?	~ 45,000	> 90	> 18	> 380	31,788	66.1

Table 5. Comparison of potassium models on SA and at 298 K. $\Delta p = p_{\mathrm{Hug}} - p_{298}$.

Potential	SA at $Z = 3.2$				BCC		Fluid at T_{m} and $p \approx 0$	
	p_{Hug}, GPa	p_{298}, GPa	Δp, GPa	T_{Hug}, K	d^0_{298}, g cm^{-3}	E^0_{298}, kJ mol^{-1}	d_{m}, g cm^{-3}	E_{m}, kJ mol^{-1}
Experiment	63.3	36.0	27.3	—	0.860	−82.8	0.8293	−78.5
EAM-1	63.9	24.5	39.4	31,510	0.8258	−82.06	0.8226	−80.84
EAM-2, para-potassium	–	35.8	—	> 90,000	0.8280	−82.00	0.8245	−80.84
EAM-2, $\gamma_{\mathrm{e}} = 2/3$	> 90	35.8	—	> 45,000	0.8280	−82.00	0.8245	−80.84
EAM-2, $\gamma_{\mathrm{e}} = 0$	66.1	35.8	30.3	31,790	0.8280	−82.00	0.8245	−80.84

ties of potassium models on the shock adiabat and at 298 K built with different EAM potentials. Clearly, the option with EAM-2 and condition $\gamma_e = 0$ provides good agreement with experiment in all the states considered.

It can be concluded that the corrected EAM-2 potential permits, in principle, adequately predicting potassium properties both on the SA and at the 298-K isotherm.

The authors of [77] calculated Li, Na, and K pressure isotherms at 298 K up to 10 GPa by the pseudopotential method (with the Heine–Abarenkov pseudopotentials). The parameters of the pseudopotentials were adjusted according to the shape of these isotherms. As a result, excellent agreement with experiment was obtained not only for crystalline but also for liquid metals near the melting points. The theory predicts a maximum of the potassium melting line at 520 K and 5.5 GPa. The calculated pressure on the lithium SA is overestimated compared with the real values, underestimated on the sodium SA, and agrees with experiment on the potassium SA. Taking into account/disregarding electron contributions has little effect on the calculated pressure on the potassium SA, in accordance with the data in Table 4.

4.2 Rubidium tandem

The pair contribution to the EAM potential of rubidium was calculated in [73, 78] using the Schommers algorithm [9] from the form of the pair correlation function of liquid rubidium. It is shown in Fig. 9. The pair contribution provides very good agreement with the diffraction PCF of liquid rubidium near the melting point (Fig. 10).

In the case of rubidium, experimental data are available for both static and shock compression. The shock compression of rubidium was studied in [24, 25, 79] up to a pressure of 39 GPa, at $Z < 3.0$. These data were used in [8, 73] to calculate the EAM-1 potential of rubidium, taking into account the thermal contributions of electrons to the energy and pressure according to MFE. The parameters of the EAM-1 potential are also given in [7]. It describes the pressure along the adiabat at $Z < 3.0$ with a relatively small mean deviation of 1.06 GPa. The calculated values of cold pressure of rubidium models at 298 K obtained by the MD method with the EAM-1 potential are presented in Table 6. They are very similar to the actual ones [75], and the MSD of the calculated pressures at 298 K from the static data at $Z < 3.0$ is 3.34 GPa. Column 7 in Table 6 shows the cold pressure values obtained in [80] using the standard method without regard for electron contributions. They are somewhat lower than those obtained by the MD method, and the difference between pressures ($\sim$ 5 GPa at $Z = 3.4$) is smaller than in the case of potassium.

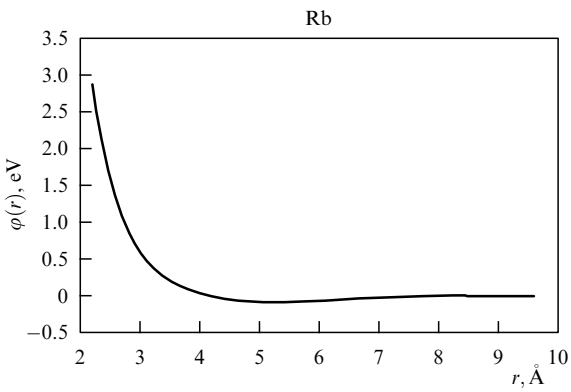

Figure 9. Pair contribution to the rubidium potential [73, 78].

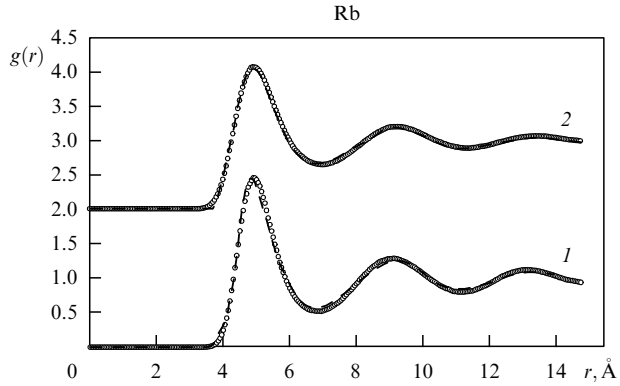

Figure 10. Pair correlation functions of liquid rubidium. *1* — 323 K, *2* — 473 K. Dashed lines — diffraction data [71], markers — MD method.

Table 6. Properties of bcc rubidium models on SA and at 298 K. EAM-1 potential. $V_0 = 55.86$ cm^3 mol^{-1}.

Z	Shock compression			Cold pressure p_{298}, GPa		
	Experiment p_{Hug}, GPa [25, 79]	EAM-1 [7, 73]		Experiment [75]	EAM-1	Standard method [80]
		T_{Hug}, K	p_{Hug}, GPa			
1	2	3	4	5	6	7
1.6	–	826	1.8	2.08	2.42	2.3
1.8	4.69	1448	4.9	3.16	3.72	3.5
2.0	7.80	2601	7.9	4.44	5.41	5.0
2.2	10.6	4478	11.4	5.01	7.00	6.7
2.4	15.3	7273	16.5	7.58	8.84	8.7
2.6	24.2	11,180	25.5	9.45	11.09	10.8
2.8	39.7	16,393	41.4	11.51	13.91	13.2
3.0	—	—	—	13.76	17.22	15.7
3.2	—	—	—	16.21	21.33	18.5
3.4	—	—	—	18.82	26.44	21.4

Static data for rubidium were obtained in [75] at pressures up to 20 GPa. The data are described by equation (8) for the values of the parameters $V_{00} = 55.86$ cm^3 mol^{-1}, $m = 5$, $n = 3$, $K_0 = 1.92$ GPa, $K_1 = 3.42$; they are shown in the 5th column of Table 6 and in the 2nd column of Table 7. In the case of rubidium, the MD calculation using EAM-1 (the 6th column of Table 6) slightly overestimates cold pressure in comparison with the static compression data. Worth mentioning here is the difference between model (bcc) and real (fcc or bct) rubidium structures. Here too, the pressure of the models weakly depends on the structure. Regarding the bcc rubidium model at 298 K and $Z = 2.5$, the pressure is 9.96 GPa; in the fcc model, it is 9.65 GPa.

By analogy with the case of potassium, the EAM-2 potential of rubidium can be calculated from the data for the 298-K isotherm [75]. The parameters of the EAM-2 potential are the same as those of the EAM-1 potential, except for the new values: $\rho_6 = 1.15$, $\rho_7 = 3.70$, $c_7 = 0.022$, $c_8 = -0.003$, $m = 2.0$, $n = 3.5$. The calculated pressure values for bcc rubidium with the EAM-2 potential at the 298-K isotherm are presented in column 3 of Table 7. The agreement of these data with experiment (2nd column) is fairly good (MSD is only 0.41 GPa).

Similarly to the case of potassium, three series of rubidium models with the EAM-2 potential were built: one ignoring electron contributions, another (para-rubidium) taking them into account in the free electron model ($\gamma_e = 2/3$), and the

Table 7. Properties of bcc rubidium models at 298 K and SA calculations. EAM-2 potential. $V_0 = 55.86$ cm^3 mol^{-1}.

Z	Pressure at 298 K, GPa		SA, EAM-2 potential								
			Experiment $p_{\rm Hug}$, GPa [25, 79]	Para-rubidium		$\gamma_{\rm e} = 2/3$				$\gamma_{\rm e} = 0$	
	Experiment [75]	EAM-2		$T_{\rm Hug}$, K	$p_{\rm Hug}$, GPa	$T_{\rm Hug}$, K	$p_{\rm Hug}$, GPa	$p_{\rm eT}$, GPa	$E_{\rm eT}$, kJ mol^{-1}	$T_{\rm Hug}$, K	$p_{\rm Hug}$, GPa
1	2	3	4	5	6	7	8	9	10	11	12
1.6	2.08	2.15	—	512	2.19	507	2.20	0.003	0.12	493	2.19
1.8	3.16	3.14	4.69	—	—	—	—	—	—	—	—
2.0	4.44	4.28	7.80	2636	6.2	2249	6.1	0.076	3.20	2202	5.95
2.2	5.01	5.94	10.6	6603	12.1	5478	11.8	0.444	16.93	4883	11.07
2.4	7.58	7.57	15.3	11,212	16.7	8252	15.7	0.98	34.4	7126	13.9
2.6	9.45	9.74	24.2	18,970	24.2	13,309	23.2	2.42	77.9	10,414	19.2
2.8	11.51	11.81	39.7	31,100	35.3	20,320	33.5	4.74	141.9	17,538	25.0
3.0*	13.76	14.16	—	—	—	—	—	—	—	—	—
3.2*	16.21	16.75	—	> 70,000	?	45,580	68.6	15.86	415.4	24,520	39.2
3.4*	18.82	19.26	—	?	?	—	—	—	—	—	—

* Extrapolation.

Table 8. Comparison of rubidium models on SA and at 298 K.

Potential	$Z = 2.8$				298 K		Fluid at $T_{\rm m}$ and $p \approx 0$	
	$p_{\rm Hug}$, GPa	p_{298}, GPa	Δp, GPa	$T_{\rm Hug}$, K	d^0_{298}, g cm^{-3}	E^0_{298}, kJ mol^{-1}	$d_{\rm m}$, g cm^{-3}	$E_{\rm m}$, kJ mol^{-1}
Experiment	39.7	11.5	28.2	—	1.530	−74.7	1.4785	−72.06
EAM-1	41.2	13.9	27.3	16,393	1.528	−75.23	1.483	−72.49
EAM-2, para-rubidium	35.3	11.8	23.5	31,100	1.519	−75.20	1.482	−72.44
EAM-2, $\gamma_{\rm e} = 2/3$	33.5	11.8	21.7	20,320	1.519	−75.20	1.482	−72.44
EAM-2, $\gamma_{\rm e} = 0$	25.0	11.8	13.2	17,538	1.519	−75.20	1.482	−72.44

third considering only the contribution to the energy ($\gamma_{\rm e} = 0$). Based on these data, the SA of rubidium was calculated, the results are presented in Table 7. The transition from a real metal to para-rubidium is accompanied by a slight decrease in the pressure on SA. Taking into consideration the electron contributions resulted in a further reduction in the pressure to $\gamma_{\rm e} = 2/3$ and then to $\gamma_{\rm e} = 0$, as in the case of potassium.

In the case of para-rubidium at $Z = 2.8$ near 30,000 K, the Grüneisen coefficient is $\gamma = 0.737$. Choosing $\gamma_{\rm e} = 0.667$ gives $\gamma_{\rm e} < \gamma$, and the inclusion of electron corrections leads to a decrease in the SA pressure in accordance with the data in Table 7.

Let us estimate the degree of agreement between experimental static and shock compression data for rubidium. It should be borne in mind that the experimental static data were obtained up to a pressure of 20 GPa, and shock data up to 40 GPa. The EAM-1 potential reproduces the shock adiabat with the MSD pressure $D_{\rm Hug} = 1.06$ GPa. The EAM-2 potential reproduces the 298-K isotherm with MSD $D_{\rm cold} = 0.41$ GPa. As with potassium, the values of $D_{\rm Hug}$ and $D_{\rm cold}$ are small and characterize a good fit of the EAM potentials. The mean standard deviation of calculated cold pressure with the EAM-1 potential versus the actual pressure on the isotherm (6th and 5th columns of Table 6) is $\Delta_{\rm cold} = 3.34$ GPa. The standard method gives $\Delta_{\rm cold} = 1.58$ GPa. The mean standard deviation of the calculated SA pressure with the potential EAM-2 and $\gamma_{\rm e} = 2/3$ (see Table 7) from the actual pressure on the SA is $\Delta_{\rm Hug} = 2.96$ GPa, and the MSD at $\gamma_{\rm e} = 0$ is $\Delta_{\rm Hug} = 7.02$ GPa. The relatively small value of $\Delta_{\rm Hug}$ at $\gamma_{\rm e} = 2/3$ means that the experimental data are consistent, and the form of the EAM potential is acceptable at $\gamma_{\rm e} = 2/3$.

Table 8 compares the properties of rubidium models on the SA and at 298 K constructed with various potentials. Clearly, variants with EAM-1 (in MFE) and EAM-2 (with the condition $\gamma_{\rm e} = 2/3$) allow good agreement to be obtained with experiment in all considered states.

The examples of potassium and rubidium indicate that it is impossible to reconcile the experimental static and shock compression data without correcting EAM potentials. The use of the free electron model to calculate the electron contributions to the energy and pressure allows approximate agreement to be reached. In the case of potassium, the best result is obtained with the use of the EAM-2 potential in the $\gamma_{\rm e} = 0$ variant, and in the case of rubidium by using EAM-1 and EAM-2 potentials with $\gamma_{\rm e} = 2/3$.

4.3 Aluminum tandem

In the case of aluminum, both static and shock compression experimental data are available. Data on shock compression of a compact metal up to pressures of ~ 260 GPa are given in Table 9 [24, 25, 81, 82]. Experimental data on the static compression of aluminum at pressures up to 125 GPa are well described by the Birch–Murnaghan equation (7), where $Z = V_0/V$, $V_0 = 9.807$ cm^3 mol^{-1}, $K_0 = 84.93$ GPa, and $K_1 = 3.79$ [83, 84]. They are shown in Table 10.

The EAM potential for fcc aluminum has been proposed in many publications [2, 4, 7, 17, 85–92]. Their authors did not calculate electron contributions to the energy and pressure (i.e., in our notations, they modeled para-aluminum). In Ref. [92], the potential was calculated using *ab initio* data, and the proposed EAM potential of aluminum had a somewhat steeper repulsive branch than the real potential; it

Table 9. Properties of para-Al and Al models on SA and at 298 K. EAM-1 and EAM-2 potentials. $V_0 = 9.993$ cm^3 mol^{-1}.

Z	Shock compression						Cold pressure, 298 K, GPa			
	Experiment [24, 81, 82]		Para-Al, EAM-1 [85]		EAM-2 [7]		Experiment [83, 84]	EAM-1 [85] at $T = 0$	EAM-2	Standard method [81]
	T_{Hug}, K	p_{Hug}, GPa	T_{Hug}, K	p_{Hug}, GPa	T_{Hug}, K	p_{Hug}, GPa				
1	2	3	4	5	6	7	8	9	10	11
1.00[a]	298	0.0	298	0.23	298	0.23	0	0.03	0.26	0.0
1.10[a]	348	8.8	325	10.45	325	10.48	9.7	10.8	10.35	7.8
1.20[a]	488	20.8	425	21.86	405	21.76	21.9	19.1	19.86	19.7
1.30[a]	818	37.2	830	35.3	843	35.68	36.6	31.9	31.85	34.5
1.40[a]	1476	58.8	1590	58.5	1500	58.97	53.9	53.0	51.73	51.9
1.50[a]	2640	86.6	2790	86.6	2619	88.26	73.9	81.1	78.77	72.7
1.60[a]	4410	121.5	4590	118.6	3430	122.1	96.7	105.3	103.2	97.0
1.70	6790	164.5	6130	160.7	5520	164.0	122.2	129.0	134.3	125.0
1.75	8180	189.3	7850	186.7	6940	189.4	136.0[b]	139.4	149.0	140.0
1.80	9670	216.5	9780	215.6	8580	218.21	150.5[b]	162.4	166.8	157.0
1.8182	—	226.9[b]	10,600	227.6	9100	228.55	—	—	—	—
1.873	—	260.6[b]	12,510	260.8	10,650	261.9	—	173.4	—	—

[a] fcc structure, [b] inter/extrapolation.

Table 10. Properties of aluminum models at 298 K and SA calculations. EAM-3 potential.

Z	Pressure at 298 K, GPa		Shock compression, EAM-3						
			Experiment p_{Hug}, GPa [81, 82]	Para-Al		$\gamma_e = 2/3$		$\gamma_e = 0$	
	Experiment [83, 84]	EAM-3		T_{Hug}, K	p_{Hug}, GPa	T_{Hug}, K	p_{Hug}, GPa	T_{Hug}, K	p_{Hug}, GPa
1	2	3	4	5	6	7	8	9	10
1.00[a]	0	0.20	0.0	298	0.23	298	0.23	298	0
1.10[a]	9.7	10.27	8.8	351	10.53	351	10.53	351	10.5
1.20[a]	21.9	21.84	20.8	485	22.78	482	22.77	468	18.9
1.30[a]	36.6	36.29	37.2	872	39.9	871	39.85	871	39.8
1.40[a]	53.9	54.49	58.8	1811	63.8	1672	63.1	1679	63.2
1.50[a]	73.9	75.23	86.6	2616	84.6	2497	84.3	2493	84.0
1.60[a]	96.7	97.60	121.5	3820	111.5	3600	111.0	3587	110.4
1.70	122.2	123.14	164.5	5405	148.2	5134	145.5	5120	144.6
1.75	136.0[b]	135.68	189.3	6652	172.0	6193	166.6	6170	165
1.80	150.5[b]	146.08	216.5	8659	204.3	7102	195.6	7107	194

[a] fcc structure, [b] extrapolation.

overestimated pressure on the Hugoniot adiabat. Therefore, the correction for the potential [92] was calculated in Refs [7, 8, 85]. The embedding potential $\Phi(\rho)$ in [92] is a smooth function of effective electron density ρ; it becomes equal to -2.6358 at $\rho \geqslant 1.20$. In Refs [7, 8, 85], the following formula was used for the embedding potential at $\rho \geqslant 1.20$:

$$\Phi(\rho) = -2.6358 + a(\rho - 1.2)^b H(\rho - 1.2)\,, \qquad (15)$$

with the optimal values of parameters $a = -1.301$ and $b = 2.500$. Here, the Heaviside function $H(z) = 1$ at $z > 0$ and $H(z) = 0$ at $z \leqslant 0$. Taking into account this potential (called EAM-1), the pressures on the para-aluminum SA were calculated. They are shown in column 5 of Table 9. They agree fairly well with experiment (column 3, the MSD of calculated and measured pressures is 1.95 GPa), which suggests the adequacy of the EAM-1 potential for describing para-aluminum.

To elucidate the role of electron contributions, similar calculations of the Al embedding potential were carried out in [7] based on shock compression data taking account of electron contributions to the MFE (EAM-2 potential) at $\gamma_e = 2/3$ using the method described in [7, 8]. The concentration of collectivized electrons was assumed to be equal to 3 electrons per atom. The correction for potential [92] had the same form (15), but $a = -0.900$. The results of calculations with the EAM-2 are presented in Table 9 and Fig. 11. They are also in excellent agreement with experiment (columns 3 and 7,

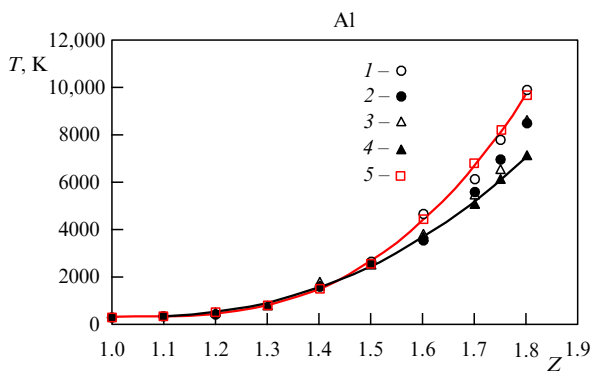

Figure 11. Temperature on Al shock adiabats. *1* — EAM-1 potential, *2* — EAM-2 potential taking into account electron contributions, *3* — EAM-3 potential disregarding electron contributions, *4* — EAM-3 potential taking into account electron contributions, *5* — standard calculation [81].

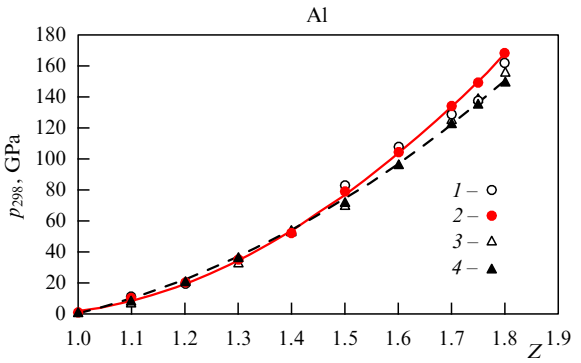

Figure 12. Cold pressure of aluminum. *1* — para-aluminium [85], *2* — aluminum models taking into account electron contributions [7], *3* — standard calculation based on shock compression data without taking account of electron contributions [81], *4* — static compression (Birch–Murnaghan equation (7)).

MSD = 1.12), which means that the EAM-2 is suitable for describing aluminum, taking into account thermal electron contributions. Consideration of these contributions markedly reduces calculated adiabat temperatures T_{Hug} (by roughly 1000 K at $Z = 1.800$; see column 6 and Fig. 11).

Figure 12 and Table 9 show the values of cold pressure calculated by the MD method on aluminum models with EAM-1 and EAM-2 potentials and by the standard method [81]. All calculations using shock data overestimate the cold pressure relative to the static data. When electron contributions are taken into consideration, the calculated cold pressure increases.

We calculated the potential (EAM-3) which best describes the static data for aluminum at 298 K. This potential has the same form as the EAM-1, but with a slightly different correction:

$$\Phi(\rho) = -2.6358 + a(\rho - 1.36)^b H(\rho - 1.36)\,, \qquad (16)$$

and optimal values of the parameters $a = -1.600$ and $b = 1.700$. The degree of agreement between the calculated cold pressure and the static data [83, 84] is illustrated by Table 10 (columns 2 and 3). The standard deviation between the calculated and experimental data is 0.73 GPa.

Using the EAM-3 potential, it is possible to calculate the corresponding SA by the graphical method described in a preceding paragraph. The results of these calculations are shown in Table 10. Calculations using static data underestimate the shock adiabat pressure relative to its actual value. The degree of such underestimation at $Z > 1.5$ is 10–12%.

These calculations can also be carried out taking into account electron contributions to the energy and pressure. The results are presented in Table 10. Consideration of the electron contributions to the energy and pressure for the case of $\gamma_{\mathrm{e}} = 2/3$ further diminishes the calculated SA, although this effect is not too large. Greater electron contributions affect temperature. Taking them into consideration results in an additional drop in temperature at $Z = 1.8$ by 1500 K, or approximately 17%. Figure 11 shows temperatures on the aluminum SA calculated with the use of various potentials. The highest temperatures were obtained by standard calculations without taking account of electron contributions [81], and the lowest ones by using the EAM-3 potential and disregarding electron contributions. The difference between these data at $Z = 1.8$ is $\sim 30\%$.

Let us estimate the degree of agreement between experimental data on the static and shock compression of aluminum. It should be taken into account that the experimental static data were obtained up to a pressure of 125 GPa, and shock data up to 260 GPa. The potentials EAM-1 (excluding electron contributions) and EAM-2 (taking them into account, at $\gamma_{\mathrm{e}} = 2/3$) were found from the shape of the aluminum SA, and the EAM-3 was calculated from the shape of the compression isotherm at 298 K. It follows from Tables 9 and 10 that the calculated EAM potentials are quite adequate in the region where they are determined. However, when the calculated cold pressure with the EAM-1 potential is compared with its actual values on the 298-K isotherm (columns 9 and 8 in Table 9, $p \leqslant 125$ GPa), the MSD $\Delta_{\mathrm{cold}} = 5.05$ GPa; at $p = 125$ GPa, the EAM-1 potential gives an error of 5.6%. In the case of the EAM-2 potential, $\Delta_{\mathrm{cold}} = 5.53$ GPa. The standard method [81] (excluding electron contributions) gives the standard deviation $\Delta_{\mathrm{cold}} = 1.82$ GPa. Thus, taking into account electron contributions has a relatively weak effect on aluminum cold pressure.

On the other hand, calculation of the aluminum SA with the use of the EAM-3 potential leads to the MSD $\Delta_{\mathrm{Hug}} = 7.15$ GPa between calculated and real pressures on the SA (at $p \leqslant 125$ GPa) in the case of para-aluminum. At the EAM-3 potential and $\gamma_{\mathrm{e}} = 2/3$, $\Delta_{\mathrm{Hug}} = 7.98$ GPa; $\Delta_{\mathrm{Hug}} = 8.36$ GPa if $\gamma_{\mathrm{e}} = 0$. Here, the calculated pressure is underestimated compared with its actual value at $Z > 1.5$, taking into account or ignoring electron contributions having but a small effect on the result. Δ_{cold} and Δ_{Hug} values are close to each other, as in the case of potassium and rubidium.

An analysis of the data presented in Tables 9–11 gives evidence that the best (even if moderate) agreement with experiment for pressures on the SA and at 298 K is obtained with the EAM-1 potential. It can probably be improved by selecting an EAM potential of a different form.

4.4 Iron tandem

There are experimental data for both the static and shock compression of iron. The analysis of shock compression below is based on the results of Refs [25, 42, 43, 45, 81, 93]. Table 12 presents data on the pressure of real iron on the principal SA (column 2). Static compression of iron in diamond cells at pressures up to 360 GPa and 200 GPa is reported in [35] and [22, 23, 94] respectively. The equation of state (8) for real hcp iron (hcp stands for hexagonal close-packed structure) is fulfilled at 298 K if the following parameters are chosen: $V_{00} = 6.73$ cm^3 mol^{-1}, $m = 2$, $n = 1$, $K_0 = 160.2$ GPa, $K_1 = 5.82$ [35]. This equation is valid at pressures up to 300 GPa or more (see the 5th column of Table 12). Other parameters were proposed in [22]: $V_{00} = 7.08$ cm^3 mol^{-1}, $m = 2$, $n = 1$, $K_0 = 165$ GPa, $K_1 = 5.47$.

A number of EAM potentials have been proposed to describe the properties of iron [2, 5, 14, 55, 68]. In [14, 55], the potential (2) was applied with parameters $\varepsilon = 0.0173$ eV, $C = 24.939$, $a = 3.4714$ Å, $m = 4.788$, $n = 8.137$.

We performed further calculations using the EAM-2 potential of iron found from the SA shape without regard for electron contributions (i.e., the para-iron potential) [7, 95]. In this potential, the iron $\Phi(\rho)$ function from Ref. [68] is piecewise continuously extended to the region of high effective electron density ρ according to the formula

$$\Phi_i(\rho) = a_i + b_i(\rho - \rho_i) + c_i(\rho - \rho_i)^{q_i} \quad \text{at} \quad \rho_i < \rho < \rho_{i+1}\,. \qquad (17)$$

Table 11. Comparison of aluminium models on SA and at 298 K.

Potential	$Z = 1.7$				fcc, 298 K		Fluid at T_m and $p \approx 0$	
	p_{Hug}, GPa	p_{298}, GPa	Δp, GPa	T_{Hug}, K	d^0_{298}, g cm^{-3}	E^0_{298}, kJ mol^{-1}	d_m, g cm^{-3}	E_m, kJ mol^{-1}
Experiment	164.5	122.2	42.3	6790	2.700	−323.8	2.377	−295.0
EAM-1	160.7	132.9	27.8	6130	2.701	−316.8	2.349	−288.45
EAM-2	164.0	134.3	29.7	5520	2.693	−316.8	2.350	−288.54
EAM-2, Para-aluminium	148.2	123.1	25.1	5405	2.693	−316.80	2.350	−288.53
EAM-3, $\gamma_e = 2/3$	145.5	123.1	22.4	5134	2.693	−316.80	2.350	−288.53
EAM-3, $\gamma_e = 0$	144.6	123.1	21.5	5120	2.693	−316.80	2.350	−288.53
[17]	187.1	137.5	49.6	7451	2.642	−310.14	2.313	−283.9

Table 12. Properties of fcc para-iron models with the EAM-2 potential [7, 95] on SA and at 298 K and with the EAM-2el potential [7] on SA. $V_0 = 7.093$ cm^3 mol^{-1}.

Z	Shock compression			Cold pressure, 298 K, GPa		Shock compression, EAM-2el [7]			
	Experiment p_{Hug}, GPa [25, 42, 43, 45, 81, 93]	EAM-2 [7, 95]		Experiment [22, 23, 35, 94, 96]	EAM-2 [7]	T_{Hug}, K	E_{eT}, kJ mol^{-1}	p_{eT}, GPa	γ_e
		T_{Hug}, K	p_{Hug}, GPa						
1	2	3	4	5	6	7	8	9	10
1.0	0	298	0	0	0.91	298	0	0	—
1.1	14.0	430	14.3	9.7	14.8	330	0.10	—	—
1.2	35.1	580	36.1	31.8	30.6	417	0.38	0.17	—
1.3	68.6	953	69.1	62.1	49.2	937	3.38	2.58	—
1.4	118.3	1946	117.7	101.3	82.1	1930	12.53	5.24	2.12
1.5	188.1	4070	186.4	150.2	140.3	3534	31.05	11.5	1.75
1.6	281.7	7930	279.6	209.4	221.3	6116	67.79	20.9	1.37
1.7	403.1	14,250	401.9	279.5	307.9	10,012	143.9	38.0	1.10
1.8	555.9	23,840	557.6	361.0	375.4	15,655	268.3	62.6	0.92

The following parameters are used here:

Interval ρ	ρ_i	a_i	b_i	c_i	q_i
38.0 – 60.0	38.0	−6.675404	−0.108005	0.00275	1.73
> 60.0	60.0	−8.473783	−0.062574	−0.00020	1.80

At high pressures, real iron has a hexagonal close-packed (hcp) structure, but the fcc structure can be used in modeling as technically more suitable for the MD method, since fcc and hcp models have very similar properties. Table 12 contains characteristics of fcc para-iron models on the SA (columns 3 and 4) constructed with the EAM-2 potential and parameters from (17). A comparison of the data for real and calculated adiabats shows that the EAM-2 potential rather accurately describes the behavior of iron on the SA, with the MSD between theoretical and measured pressures (columns 2 and 4) being only 1.22 GPa.

However, results of calculations of fcc para-iron pressure with the EAM-2 potential at 298 K reveal alternating deviations from those measured in a static experiment. Here, the MSD between theory and experiment (columns 6 and 5) is rather large (around 14 GPa).The authors of [42] calculated, based on shock compression data, the cold pressure function at 0 K by the standard method, disregarding electron contributions. At $Z > 1.5$, the cold pressure was 30–60 GPa below that shown in Table 12 and 20–40 GPa below the static values reported in [22, 23, 35, 94, 96]. This means that the transition from a real SA to the cold pressure function taking no account of electron contributions results in a significant reduction in the pressure. As was mentioned above, consideration of thermal electron contributions must increase cold pressure.

Thus, the excellent agreement between calculated and actual pressures on the SA when using the EAM-2 potential does not necessarily mean agreement with experiments on cold pressure, heat capacity, etc. It should be clarified whether the agreement can be improved by including electron contributions. Reference [7] considers the possibility of using the EAM-2 potential to describe iron models with the addition of thermal electron contributions E_{eT} and p_{eT} to the obtained values of model energy and pressure, respectively. For each Z value, a new temperature on the T_{Hug} adiabat was found self-consistently from the condition that the sum of the energy of the model with the EAM-2 potential and the electron energy E_{eT} from Refs [56, 57] at this T_{Hug} value is equal to the actual energy on the adiabat. The difference between the actual pressure of iron on the adiabat and the model pressure was assumed to be equal to the thermal contribution p_{eT} of electrons to the pressure. This version of iron description will be called EAM-2el.

Results of these calculations are presented in Table 12. Taking into account electron contributions markedly decreases the temperature on the adiabat (by 35% at $Z = 1.8$). The calculated values of p_{eT} and E_{eT} can be used to find out the electronic Grüneisen coefficient $\gamma_e = p_{eT}V/E_{eT}$. The γ_e values of iron models lying in the 0.9–2.1 range are higher than the value 2/3, characteristic of the MFE.

γ_e decreases monotonically during heating. The described method makes it possible to match the data on the SA and on the 298-K isotherm. As far as heat capacity is concerned, taking into account electron contributions improves the agreement with experiment. For example, the heat capacity of iron C_p during pulsed heating at 4,000 K is 44.7 J mol^{-1} K^{-1} [97], while calculation with the EAM-2el potential gives $C_V \approx 40.8$ J mol^{-1} K^{-1} (at 230 GPa).

Let us analyze, by analogy with previous examples and moving in the opposite direction, the adequacy of the EAM potential. The choice of the cold pressure function measured under static conditions [22, 23, 35, 94, 96] as the initial parameter allows calculating the corresponding EAM potential at a temperature of 298 K and constructing a series of models under shock compression. Judging by static data, the optimal parameters of the EAM potential in accordance with equation (17) have the following form:

Interval ρ	ρ_i	a_i	b_i	c_i	q_i
38.0 – 47.5	38.0	−6.512968	−0.108593	0.0088	1.4
47.5 – 60.0	47.5	−7.454893	−0.076444	−0.0020	1.2
> 60.0	60.0	−8.451876	−0.080421	−0.0081	1.1

In what follows, this potential is referred to as EAM-3. The results of calculating the properties of para-iron models with the EAM-3 potential are presented in Table 13. Column 3 gives cold pressures at 298 K calculated from models with the EAM-3 potential. They are in good agreement with experiment [35] (2nd column, MSD = 1.34). Then, characteristics of states on the shock adiabat of para-iron models with the EAM-3 potential can be calculated by the graphical method described in Section 2.2 (if pressures do not exceed the actual ones on the 'cold ' isotherm).

Column 6 of Table 13 shows calculated pressure values on the SA. They differ from those on the real iron adiabat (column 4). The 7th column shows the pressure difference Δp between the models with the EAM-3 potential and real iron on the shock adiabat. At $Z < 1.5$, these figures are small and behave randomly, but at $Z \geqslant 1.5$, the pressure of the para-iron models becomes 10–30 GPa lower than the real pressure on the SA, i.e., the SA of models with the EAM-3 potential lies below the real one.

So, taking the cold pressure function of iron as a basis, it is possible to calculate the shock adiabat of para-iron undergoing compression up to $Z = 1.5$ without taking account of thermal electron contributions with an error of $\sim 5\%$; the error increases by 2–3 times at $Z = 1.6$. Therefore, it is necessary to consider the influence of electron contributions on the properties of models built with the use of the EAM-3 potential. Table 14 shows results of a graphical calculation of the iron SA with the EAM-3 potential, taking into consideration thermal contributions of electrons. The thermal energy of electrons was calculated from the data of Refs [56, 57]. The contribution of electrons to the pressure was taken into account using the relation $p_{eT}V = \gamma_e E_{eT}$. Table 14 presents results of SA calculations with the EAM-3 potential by the

Table 13. Properties of fcc para-iron models at 298 K and on SA. EAM-3 potential.

Z	Pressure at 298 K, GPa		SA			Δp, GPa
			Experiment	EAM-3		
	Experiment [22, 23, 35, 95, 96]	EAM-3	p_{Hug}, GPa	T_{Hug}, K	p_{Hug}, GPa	
1	2	3	4	5	6	7
1.0	—	—	0	298	0.70	0
1.1	7.5	—	14.0	—	—	—
1.2	29.7	30.8	35.1	460	32	−3.1
1.3	60.2	61.1	68.6	1260	70.1	1.5
1.4	99.8	98.4	118.3	2750	124.5	6.2
1.5	149.4	148.0	188.1	4300	179	−9.1
1.6	209.4	211.9	281.7	5850	250	−31.7
1.7	280.6	280.5	403.1	12,000	371[a]	—
1.8	363.4	362.8	555.9	22,840	540[a]	—

[a] Extrapolation.

Table 14. Properties of fcc-iron models on the principal SA. EAM-3 potential taking into account electron contributions.

Z	Experiment p_{Hug}, GPa [25, 42, 43, 45, 81, 93]	EAM-3, $\gamma_e = 0$		EAM-3, $\gamma_e = 1.55$	
		T_{Hug}, K	p_{Hug}, GPa	T_{Hug}, K	p_{Hug}, GPa
1	2	3	4	5	6
1.0	0	298	0.70	298	0
1.2	35.1	400	31.8	400	32.2
1.3	68.6	970	67.1	1030	69.0
1.4	118.3	1910	117.5	2163	124
1.5	188.1	3050	170	2580	182
1.6	281.7	3630	228.6	4213	249
1.7	403.1	6020	317	7792	376[a]
1.8	555.9	9030	424	13,860	555[a]

[a] Extrapolation.

graphical method with the choice of γ_e equaling either 0 or 1.55.

Obviously, the variant with the EAM-3 potential and $\gamma_e = 0$ leads to a marked reduction in pressure at the calculated SA as compared with the real one. With the choice of $\gamma_e = 1.55$, the calculated adiabat approaches the actual one. Noticeable deviations of 20–30 GPa remain only at $Z = 1.6-1.7$. As in the case of the EAM-2 potential, taking into account the thermal contribution of electrons to the iron energy, but disregarding the contribution to pressure, leads to unacceptable errors in SA calculations.

At $Z = 1.8$, the real pressure difference on the adiabat and on the 298-K isotherm is 194.9 GPa (see Table 12, columns 2 and 5). In the case of the EAM-2 potential, it is equal to 182.2 GPa (columns 4 and 6). In the case of the EAM-3 potential, this pressure difference is 177.2 GPa for para-iron (see Table 13, columns 3 and 6), 61.2 GPa for iron at $\gamma_e = 0$ (Table 14, column 4), and 192.2 GPa at $\gamma_e = 1.55$ (Table 14, column 6). The best agreement with experiment with respect to the pressure difference is obtained in the EAM-2 and EAM-2e1 variants, as well as EAM-3 at $\gamma_e = 1.55$.

The calculated temperatures on the adiabat at $Z = 1.8$ are 23,840 K with the EAM-2 potential at electron contributions, 15,655 K with the EAM-2el potential, taking into consideration electron contributions, 22,840 K with the EAM-3 potential, without taking account of electron contributions, 9030 K with the EAM-3 potential and due regard for electron contributions at $\gamma_e = 0$, and 13,860 K at $\gamma_e = 1.55$. Temperature plots along the principal shock adiabat of iron are shown in Fig. 13.

What are the possible causes of the discrepancy with experiment? (1) The experimental data on cold pressure and the shock adiabat disagree; (2) the data on the thermal energy of iron electrons are incorrect; (3) the EAM potential found from the cold pressure function is inaccurate; (4) the interparticle potential of iron changes during heating above 10,000–20,000 K. The very fact that there is a change in the effective interparticle potential at high temperatures could be verified by calculations using the *ab initio* method. Apparently, the accuracy of the calculation of electronic properties is sufficient for this purpose. Indeed, in the case of nickel at $T = 40{,}000$ K, the calculated heat capacities C_V proved close to the real ones; specifically, 34.1 J mol^{-1} K^{-1} in [56, 57] and 35.7 J mol^{-1} K^{-1} in [59].

The potential from Ref. [55] greatly overestimates the pressure and energy of the bcc iron model at 298 K and standard density 7.873 g cm^{-3}. At the same time, it underestimates fluid density and overestimates its energy at the melting temperature T_m. For example, the real iron density at

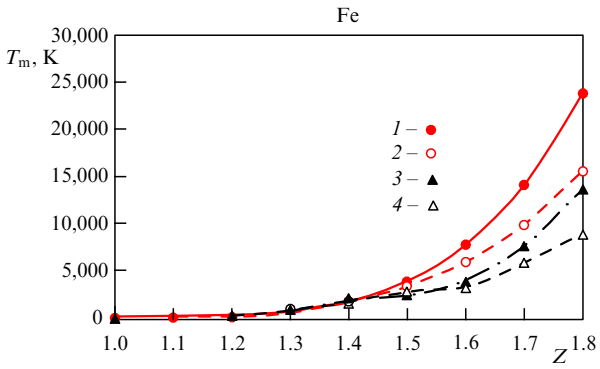

Figure 13. Temperature on calculated iron shock adiabats. *1* — EAM-2 potential for para-iron, *2* — EAM-2el potential taking into consideration thermal contributions of electrons to the energy and pressure [7], *3* — EAM-3 potential for iron taking account of electron contributions at $\gamma_e = 0$ [7], *4* — EAM-3 potential taking into account electron contributions at $\gamma_e = 1.55$ [7].

2500 K is 6.397 [98] and model density at $p \approx 0$ is 4.32 g cm^{-3}. With such initial data, it makes no sense to calculate the iron SA.

A comparison of the properties of models with different potentials (Table 15) shows that none of the options considered for the description of a metal affords good results for the iron tandem. Apparently, the main cause is the lack of information about the behavior of the electronic subsystem. Correction of these data could improve the agreement with experiment of the calculated properties with EAM-2 and EAM-2el potentials.

4.5 Nickel tandem

Similar calculations can be made with another transition metal, nickel. Shock compression of compact and porous Ni has been investigated by many authors [24]. In what follows, we shall use data obtained for compact nickel at pressures up to $\sim$ 760 GPa [24–26, 40]. Static compression of nickel under 150 GPa was investigated in Refs [22, 23]. The cold pressure isotherm at 298 K is described by Eqn (8) at $m = 2$, $n = 1$, $V_{00} = 6.589$ cm^3 mol^{-1}, $K_0 = 176.7$ GPa, and $K_1 = 5.23$ [23].

There are a large number of publications on the modeling of crystalline nickel using the MD method. Early authors used potentials calculated from the known structural diffraction data to model liquid nickel with the use of the Percus–Yevick equation [99] or the Born–Green–Bogolyubov equation [100]. This approach can be used to achieve good agreement between the PCF of the model and the diffraction PCF, but usually the energy of the model differs several-fold from the actual one. Later, EAM potentials were proposed for fcc [4, 88, 101–106] and liquid [60, 67, 107, 108] nickel.

Table 15. Comparison of fcc-iron models on SA and at 298 K.

Potential	$Z = 1.6$				bcc at 298 K and $p \approx 0$		Fluid at T_m and $p \approx 0$	
	p_{Hug}, GPa	p_{298}, GPa	Δp, GPa	T_{Hug}, K	d^0_{298}, g cm^{-3}	E^0_{298}, kJ mol^{-1}	d_m, g cm^{-3}	E_m, kJ mol^{-1}
Experiment	281.7	209.4	72.3	—	7.873	−407.8	6.999	−366.6
EAM-2	279.6	221.3	58.3	7930	7.938	−407.0	7.054	−348.1
EAM-2el	279.6	221.3	58.3	6160	7.938	−407.0	7.054	−336.8
EAM-3	250.0	211.9	38.1	5812	7.938	−407.1	7.056	−348.2
[68]	231.0	159.4	71.6	3764	7.693	−375.9	7.049	−331.0
(2) [14, 55]	—	190.1	—	—	6.791	−223.1	4.992	−174.2

Reference [108] reports excellent agreement between the structure factor of the liquid nickel model and the diffraction factor; however, the potentials proposed for fcc nickel are on the whole not good enough for the liquid metal.

In Ref. [88], the *ab initio* method was used to construct several crystal structures of nickel and to calculate the parameters of the corresponding EAM potential. The obtained potential made it possible to correctly describe basic physical properties of crystalline nickel, but it overestimates liquid nickel density at 2500–3600 K by ~ 1 g cm^{-3} and underestimates the energy by 10–20 kJ mol^{-1}. In addition, the density of liquid models turns out to be ~ 0.2 g cm^{-3} higher than that of fcc nickel.

In Ref. [7, 60], the EAM potential in the form [1] was applied to simulate liquid nickel by the MD method. However, this potential proved of little use for calculating the nickel melting line. Further calculations of the EAM potential were carried out in Ref. [109] where a different form of the pair contribution to the potential (Morse function) and the power law (instead of exponential) dependence for effective electron density were chosen. The electron contribution to the energy was described in accordance with calculations [56, 57] in which the density of nickel d-states (up to 50,000 K) was used. Reference [109] considered two variants of electron behavior. One is based on the assumption that electrons do not contribute to either energy or pressure (para-nickel, EAM-A potential), the other on the assumption that electrons contribute to the energy, but not to the pressure (i.e., $\gamma_e = 0$, EAM-B potential). Parameters of the EAM potential were selected using shock compression data [24–26]. The parameters of the nickel EAM potentials in these two cases differ only in the values of the c_8 coefficient in formulas (5) (2.71 in EAM-A and 3.48 in EAM-B). The corresponding embedding potentials are shown in Fig. 14. Both potentials are in good agreement with experiment as far as the shape of the adiabat is concerned (Fig. 15). Taking into account electron contributions leads to a decrease in the adiabat temperature from 27,360 to 16,430 K at $Z = 1.8$ (Table 16). Analytical calculations without taking into account electron contributions [47] give results for para-nickel close to our estimates (column 7 in Table 16). At the same time, the inclusion of electron heat capacity in the calculation scheme in Ref. [110] yielded good agreement with our data for nickel models constructed with due regard for electron contributions (columns 5 and 8 in Table 16). The electron thermal energy may be as high as 32% of the total metal energy.

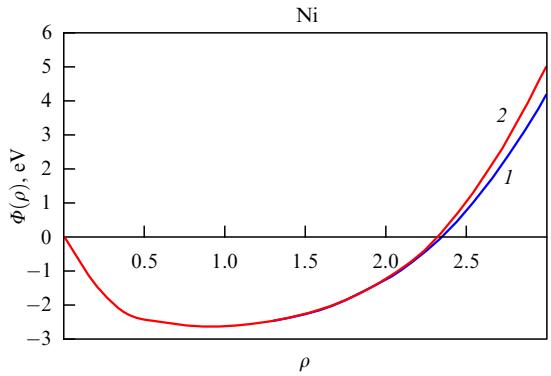

Figure 14. Nickel embedding potential. *1* — disregarding electron contributions [109], *2* — taking into account electron contributions to the energy [7, 85].

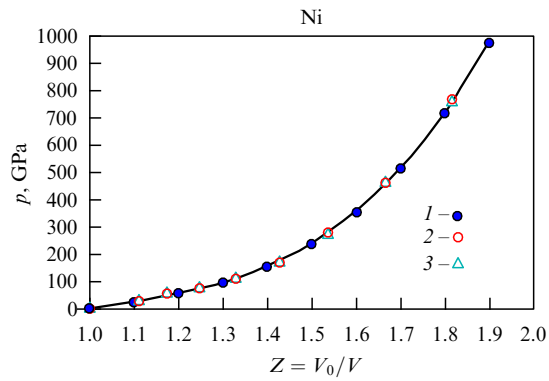

Figure 15. Nickel Hugoniot adiabat. *1* — experiment [24–26], *2* — MD calculation with the EAM-A potential (para-nickel, excluding electron contributions), *3* — MD calculation with the EAM-B potential (nickel, taking into account electron contributions to the energy). $V_0 = 6.6133$ cm^3 mol^{-1}. All data are approximated by third degree polynomials.

Table 16 shows experimental data on the static compression of nickel in diamond cells [22, 23] under pressures up to

Table 16. Properties of nickel models on SA and at 298 K. EAM-A and EAM-B potentials. $V_0 = 6.6133$ cm^3 mol^{-1}.

Z	Shock compression							Cold pressure, 298 K, GPa				
	Experiment p_{Hug}, GPa [24–26]	EAM-A [109]		EAM-B [109]		T_{Hug}, K		Experiment [22, 23]	EAM-A [109]	EAM-B [109]	[47]	[50]
		T_{Hug}, K	p_{Hug}, GPa	T_{Hug}, K	p_{Hug}, GPa	[47]	[110] [c]					
1	2	3	4	5	6	7	8	9	10	11	12	13
1.0 [a]	0	298	0	298	4.75	298	298	0	0	0	0	0
1.1 [a]	23.8	300	31.0	300	30.41	310	439	20.53	27.0	27.8	20.7	23.0
1.2 [a]	54.9	316	60.1	336	59.12	676	667	49.83	56.6	56.0	49.7	54.3
1.3 [a]	96.3	640	99.0	696	98.52	1400	1150	87.92	95.3	93.9	88.0	95.1
1.4 [a]	155.5	1490	155.8	1620	156.2	2670	2060	135.31	146.7	146.5	136.8	146.6
1.5 [a]	239.8	3500	238.6	3310	239.9	4910	3560	—	214.5	218.9	197.3	210.2
1.6 [b]	356.6	7600	355.5	6080	357.1	8710	5810	—	302.4	316.1	270.5	286.9
1.7 [b]	513.4	15,040	514.4	10,300	515.4	14,870	8980	—	414.0	443.4	357.8	377.8
1.75 [b]	609.0	20,480	612.2	13,100	612.5	19,150	—	—	479.8	519.8	407.1	—
1.8 [b]	717.4	27,360	723.6	16,430	722.6	24,410	—	—	552.9	605.6	460.3	483.8

[a] fcc-Ni, [b] bcc-Ni, [c] interpolation.

150 GPa. The construction of nickel models at 298 K makes it possible to calculate the cold pressure of nickel in various MD versions. The potentials EAM-A and EAM-B give rather similar results at $Z < 1.5$ (columns 10, 11 in Table 16), which are in good agreement with the estimates by the standard method taking into account electron contributions [50], but slightly higher than experimental data (column 9). On the contrary, the standard method without taking into account electron contributions [47] leads to good agreement with experiment. At $Z > 1.5$, the inclusion of electron contributions slightly increases the cold pressure in accordance with the general rule (see Section 2.2). At $Z = 1.8$, the difference between cold pressures in [109] and [47] reaches 145 GPa. Cold pressure plots obtained by different methods are shown in Fig. 16.

Similarly to the previous tandems, one can calculate the EAM potential of nickel from static data for compressibility at 298 K and check how suitable this potential is for describing high-temperature states. The initial energy in shock compression was assumed to be equal to the model energy at $Z = 1$ and 298 K. The resulting potential EAM-C has the same shape as EAM-A and EAM-B, but with coefficients $c_7 = 1.15$, $m = 2.40$. It can be used up to 150 GPa. The cold pressure data calculated with EAM-C are presented in Table 17.

Let us consider the calculated difference Δp between the pressure on the nickel SA and the cold pressure at 298 K using different EAM potentials. These data are shown in Table 18. They look disappointing. The best agreement with experiment in terms of pressures p_{Hug} and p_{298} was obtained using the Sutton–Chen potential [5] (Eqn (2)); however, this potential underestimates the energy of para-nickel in the standard state by ~ 40 kJ mol^{-1} (at the potential parameters indicated in [5] and in the case of its shift in accordance with

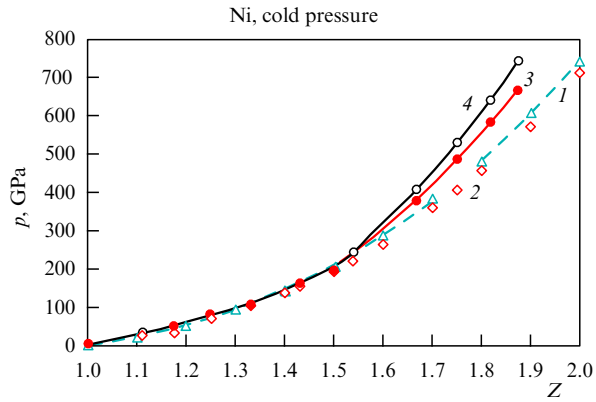

Figure 16. Nickel cold pressure. *1* — using shock compression of nickel at 0 K [50], *2* — para-nickel at 0 K [47], *3* — para-nickel at 298 K [109], *4* — nickel at 298 K [109].

$\psi(r) = 0$ at the cutoff radius $r_c = 6.0$ Å) and overestimates fluid density. The potential [16, 17] (equation (3)) gives reasonable pressure values, but greatly overestimates the energy, while underestimating fluid density. The potential [7, 101] overestimates p_{Hug} and p_{298} and leads to a minimum pressure on the isochor $Z = 1.4$ near 1500 K, i.e., it simulates an anomalous metal. Potentials EAM-A, B, C underestimate the pressure difference Δp by ~ 10 GPa with respect to experiment. None of these potentials provides good agreement with experiment for all of these reference positions. In other words, the applicability of the EAM potentials for describing nickel in a wide range of pressures and temperatures remains questionable.

Table 17. Properties of nickel models at 298 K and SA calculations. EAM-C potential. $V_0 = 6.6133$ cm^3 mol^{-1}.

Z	Pressure at 298 K, GPa		Shock compression, EAM-C						
			Experiment p_{Hug}, GPa [24–26]	Para-nickel		$\gamma_e = 0$		$\gamma_e = 1.55$	
	Experiment [22, 23]	EAM-C		T_{Hug}, K	p_{Hug}, GPa	T_{Hug}, K	p_{Hug}, GPa	T_{Hug}, K	p_{Hug}, GPa
1	2	3	4	5	6	7	8	9	10
1.0	0	0	0	—	—	—	—	—	—
1.1	20.53	21.7	23.8	—	—	—	—	—	—
1.2	49.83	49.86	54.9	439	49.9	300	49.8	—	—
1.3	87.92	87.56	96.3	873	89.6	734	89.2	—	—
1.4	135.31	135.7	155.5	2029	145.8	1771	144.3	1842	146.6
1.5	—	—	239.8	—	—	—	—	—	—

Table 18. Comparison of fcc-nickel models on SA and at 298 K.

Potential	$Z = 1.4$				fcc at 298 K and $p \approx 0$		Fluid at T_m and $p \approx 0$	
	p_{Hug}, GPa	p_{298}, GPa	Δp, GPa	T_{Hug}, K	d^0_{298}, g cm^{-3}	E^0_{298}, kJ mol^{-1}	d_m, g cm^{-3}	E_m, kJ mol^{-1}
Experiment	155.5	135.2	20.2	—	8.875	−424.8	7.839	−390.0
EAM-A	156.2	146.5	9.1	1490	8.748	−420.63	7.843	−364.5
EAM-B	155.8	146.7	9.9	1620	8.748	−420.53	7.843	−364.5
EAM-C	145.8	135.7	10.1	2029	8.756	−420.40	7.856	−364.7
[5, 13] (2)	155.4	130.47	24.9	2784	9.170	−467.33	8.041	−417.5
[16, 17] (3)	162.5	146.4	16.1	2386	8.830	−420.07	7.626	−363.7

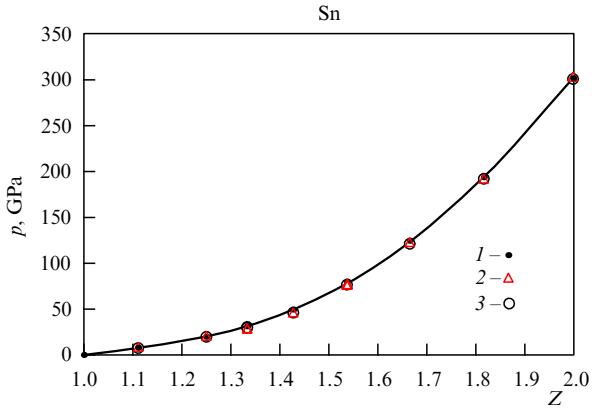

Figure 17. Tin Hugoniot adiabat. *1* — experiment [25, 26, 39], *2* — MD calculation with the EAM-A potential (para-tin, excluding electron contributions), *3* — MD calculation with the EAM-B potential (taking into account electron contributions to the energy [7, 8]). $V_0 = 16.262$ cm^3 mol^{-1}.

4.6 Tin tandem

The tin SA under pressures up to 300 GPa is shown in Fig. 17 [7, 8, 25, 26, 39]. Tin static compression in diamond cells was studied in [111] up to 200 GPa and in [112] up to 230 GPa. The dependence of pressure on the degree of compression is described in [111, 112] by the expression $p = p_0 + p(Z)$, where $p(Z)$ is given by (7) and p_0 is the initial pressure in an area with a given crystalline structure. In the section with the bcc structure (from 76 to 158 GPa), the parameters of equation (7) are as follows: $p_{76} = 76$ GPa, $V_{76} = 33.46$ Å^3 for every 2 atoms, $K_0 = 347$ GPa, $K_1 = 3.84$ [112]. For the hcp phase (158–230 GPa), the parameters are as follows: $p_{158} = 158$ GPa, $V_{158} = 27.77$ Å^3 for every 2 atoms, $K_0 = 631$ GPa, $K_1 = 4.0$. Accordingly, the values for the bcc phase in [111] are $p_{100} = 100$ GPa, $V_{100} = 15.78$ Å^3 per atom, $K_0 = 400$ GPa, $K_1 = 3.37$, and for the hcp phase $p_{100} = 157$ GPa, $V_{100} = 13.96$ Å^3 per atom, $K_0 = 652$ GPa, $K_1 = 4.0$. These data are generally in good agreement. Tin cold pressure data are presented in Table 19.

In Ref. [113], the effective pair potential of tin was calculated from the diffraction data. Tin modeling without regard for electron contributions is described in [8] (EAM-A potential), while Refs [7] (EAM-B potential) and [114] (EAM-C potential) describe it taking electron contributions into consideration. Tin was also modeled in [115–118] by the *ab initio* method. Parameters of the EAM-B potential of tin are given in [7]; specifically, formulas (5) contain $c_8 = -0.040$, $m = 1.24$, and $n = 1.50$. When electron contributions are disregarded (para-tin), it is sufficient to choose $c_8 = -0.240$ and $n = 1.80$ in potential (5) in order to obtain practically the same calculated Hugoniot adiabat (see Fig. 17).

Certain results of calculations with tin EAM-B and EAM-C potentials are presented in Table 19. The calculated pressure values on the SA are consistent with actual ones in the case of EAM-B (columns 4 and 2 in Table 19, MSD = 2.05 GPa), but less so in the case of EAM-C (MSD = 4.03 GPa). The EAM-B potential significantly underestimates cold pressure at $Z = 1.4-1.8$, the EAM-C potential overestimates pressure at $Z = 2.0$ by 30 GPa, and the results of the standard method [40] are in good agreement with static data.

It is possible to calculate the EAM potential from cold pressure data [111, 112]. This potential coincides with that given in [7], but with modified parameters: $\rho_6 = 1.20$, $\rho_7 = 2.00$, $\rho_8 = 2.94$, $c_7 = 1.054$, $c_8 = -0.18$, $c_9 = 1.425$, $m = 1.54$, $n = 6.00$, $q = 2.00$ (one more division of the ρ-axis was added). We call it EAM-D. This potential works at $\rho < 3.1$. MD calculations with the EAM-D potential are given in Table 20. The EAM-D potential overestimates the calculated pressure on the SA when taking into account electron contributions in the variant with $\gamma_e = 2/3$ as well as at $Z = 1.4-1.6$ in the variant with $\gamma_e = 0$. As a result, all the potentials (EAM-B, EAM-C, and EAM-D) overestimate the pressure difference on the SA and on the 298-K isotherm at average Z values in comparison with experiment. Possibly, agreement can be improved by using the EAM-D potential and taking a more realistic account of electron contributions.

4.7 Grüneisen coefficients

One of the options for using the cold pressure function to calculate properties at elevated temperatures includes estimating the Grüneisen coefficient $\gamma = (V/C_V)(\partial p/\partial T)_V$ from the compressibility of a solid metal at 0 or 298 K. Specifically, formulas like (12) and (13) are used to estimate the Grüneisen coefficient when calculating cold pressure by the standard method [51, 52]. The formulas can be checked based on static compression data. In this case, it is convenient to carry out the analysis using metal models, because it is this approach that makes possible an accurate calculation of pressure at 0 or 298 K, all its derivatives with respect to volume, and the coefficient γ itself. Figure 18 compares the Grüneisen coefficients found for lithium models in [7] with those calculated by formula (13). The $p(Z)$ dependence was approximated by a third degree polynomial. The actual γ value of the models depends on temperature, while formula

Table 19. Properties of tin models on SA and at 298 K. bcc-crystal. EAM-B and EAM-C potentials. $V_0 = 16.262$ cm^3 mol^{-1}.

Z	Shock compression					Cold pressure p_{298}, GPa			
	Experiment p_{Hug}, GPa [25, 26]	EAM-B		EAM-C	T_{Hug}, K				
		T_{Hug}, K	p_{Hug}, GPa	p_{Hug}, GPa	[40]	Experiment [111, 112]	EAM-B	EAM-C	[40]
1	2	3	4	5	6	7	8	9	10
1.0	0.0	298	1.0	0	298	0	1.6	1.57	0
1.2	14.4	300	13.1	17.7	—	17.5	16.6	17.2	13
1.4	42.9	1652	42.6	41.5	1450	38.3	31.5	33.7	37
1.6	97.4	5700	93.2	101.3	5360	73.0	53.6	67.0	74
1.8	184	13,665	183	185.5	11,700	122.5	102	130.5	125
2.0	300	24,000	302	308.2	20,540	187.7	178	217.5	189
2.1	367	30,480	365	—	—	226.3	223	—	226

Table 20. Properties of tin models at 298 K and SA calculations. EAM-D potential. $V_0 = 16.262$ cm^3 mol^{-1}.

Z	Pressure at 298 K, GPa		Shock compression, EAM-D						
	Experiment [111, 112]	EAM-D	Experiment p_{Hug}, GPa [25, 26]	Para-tin		$\gamma_e = 2/3$		$\gamma_e = 0$	
				T_{Hug}, K	p_{Hug}, GPa	T_{Hug}, K	p_{Hug}, GPa	T_{Hug}, K	p_{Hug}, GPa
1	2	3	4	5	6	7	8	9	10
1	0	0.98	0.0	298	0	298	0	298	0
1.2	17.5	17.7	14.4	393	15.8	392	15.8	390	15.8
1.4	38.3	38.5	42.9	1616	47.4	1500	46.6	1500	46.6
1.5	53.9	53.2	66.4	4719	82.6	4004	79.3	3901	78.0
1.6	73.0	72.5	97.4	8788	122	6870	115	6518	112
1.8	122.5	123.6	184	20,888	217	14,200	204	14,018	182
2.0	187.7	188.4	300	40,100	343	24,115	314	21,124	284

Note. bcc models are prone to amorphization.

(13) gives results independent of temperature and overestimated by almost two times.

Figure 19 shows the same data for copper models. Here, the agreement of the calculated γ values with formula (13) is better than for lithium, and formula (13) overestimates γ by an average of 20%.

One can also check the accuracy of equation (13) for calculating the Grüneisen coefficients γ from cold pressure data for aluminum. The cold pressure function of aluminum (Table 10, column 2) is very well described by the polynomial

$$p_{298}\left[\text{GPa}\right] = 9.605Z^3 + 93.007Z^2 - 130.29Z + 27.693\,.$$

Formula (13) gives γ values from 1.77 at $Z = 1.0$ to 1.21 at $Z = 1.8$ (Fig. 20, curve *2*). Calculations with the EAM-2 potential yield similar values: from $\gamma = 1.55$ at $Z = 1.0$ to $\gamma = 1.21$ at $Z = 1.8$ [7]. Direct calculations of the Grüneisen coefficient at 298 K using aluminum models with the EAM-2 potential at $Z = 1.0$ and with the EAM-3 potential give $\gamma = 1.53$ and $\gamma = 1.77$, respectively. The actual values of the Grüneisen coefficient at 350 K deviate noticeably from the predictions of formula (13). The standard calculation method based on the shock data gives $\gamma = 2.0$ at $Z = 1.05$ [81].

To conclude, calculations using formula (13) are apt to both underestimate and overestimate the value of γ. Moreover there is a tendency to overestimate the value γ in the low pressure region. In general, this formula provides only a rough estimate of the Grüneisen coefficient.

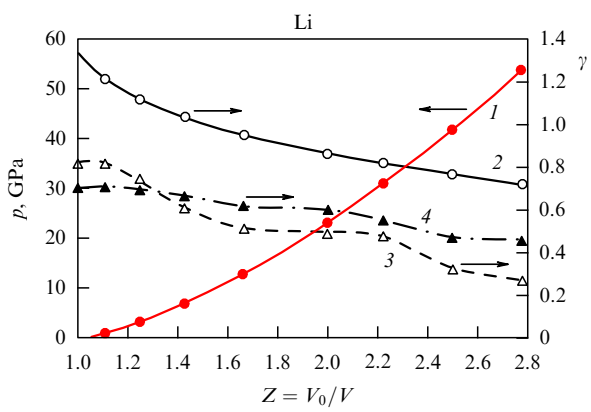

Figure 18. Grüneisen coefficients of lithium models with the EAM potential and taking into account all thermal electron contributions [7]. *1*—pressure of lithium models at 298 K [7], *2*—calculation of the Grüneisen coefficients γ according to formula (12), *3*—γ coefficients of lithium models at 700 K, *4*—γ coefficients at 4,000 K [7].

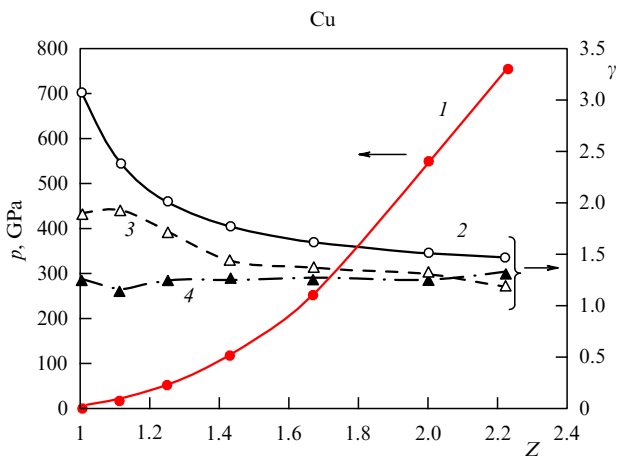

Figure 19. Grüneisen coefficients of copper models with the EAM potential taking into account thermal electron contributions [7]. *1*—pressure of copper models at 298 K [7], *2*—calculation of Grüneisen coefficients γ according to formula (12), *3*—γ coefficients for copper models at 298 K, *4*—γ coefficients at 10,000 K [7].

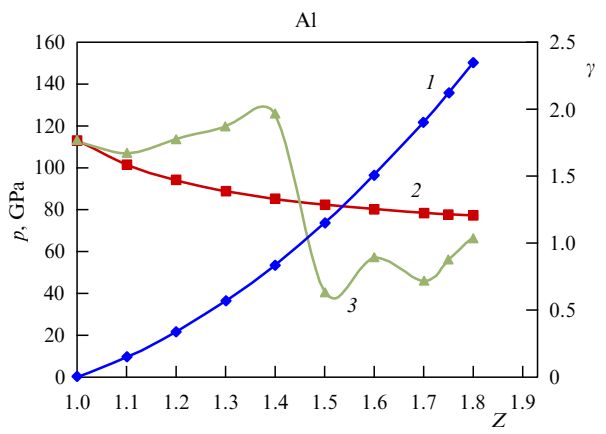

Figure 20. Grüneisen coefficients of aluminum models with the EAM-3 potential. *1*—pressure of aluminum models at 298 K [83, 84], *2*—calculation of Grüneisen coefficients γ according to formula (13), *3*—γ coefficients of aluminum models with the EAM-3 potential at 350 K.

Table 21. Pressure differences $\Delta p = p_{\mathrm{Hug}} - p_{298}$.

Metal	Z	Δp, experiment, GPa	Taking into account electron contributions	Δp, calculation from SA data, GPa	From static compression data			
					Parametal	$\gamma_e = 2/3$	$\gamma_e = 0$	$\gamma_e = 1.55$
1	2	3	4	5	6	7	8	9
K	2.8	11.6	MFE	17.6	29.4	27.8	15.7	—
Rb	2.8	28.2	MFE	27.5	23.8	22.0	13.5	—
Al	1.7	42.3	MFE	31.7	25.0	22.3	21.4	—
Fe	1.4	17.0	[56, 57]	35.6	26.1	—	—	—
Fe	1.7	123.6	[56, 57]	94.0	90.5	—	36.5	95.5
Ni	1.4	20.2	[56, 57]	9.3	10.1	—	8.6	10.9
Sn	2.0	112.3	MFE	124	154.6	125.6	95.6	—

4.8 Concluding comment

What are the possible causes of the discrepancy between theory and experiment? They are inaccurate values of initial parameters, errors arising from the complex nature of static and shock compression experiments, thermodynamic nonequilibrium of matter behind the shock front, deviations from the free electron model, and changes in the electron structure of metal atoms at high pressures and temperatures, as well as common disadvantages inherent in the embedded atom model. In an analysis of modeling studies, all these causes manifest themselves in the form of thermal electron contributions to the energy and pressure. It is especially important to verify the EAM potential when extrapolating results of calculations (e.g., of phase diagrams) to high temperatures.

Table 21 summarizes results of an analysis of applying the EAM to describe the behavior of metals in a wide range of pressures. These data show that the use of EAM potentials taking into account the thermal contributions of electrons leads in the best case to discrepancies with experiment in the values of difference $\Delta p = p_{\mathrm{Hug}} - p_{298}$ by 1–4 GPa for alkali metals, 12–20 GPa for aluminum, ~ 12 GPa for tin, ~ 30 GPa for iron, and ~ 10 GPa for nickel. Disregarding electron contributions (i.e., for parametals) results in a discrepancy with experiment by 5–42 GPa in both directions. This equally applies to the derived properties (heat capacity, thermal expansion coefficient, thermal pressure coefficient, etc.); the accuracy of predicting these properties based on the EAM is not very high. There is a tendency towards greater divergences with decreasing compressibility of metals.

As a result, one has to state that the EAM can hardly be regarded as suitable for describing the temperature dependence of metal properties. Temperature dependences in the context of the EAM are mainly due to changes in effective electron density due to thermal expansion. In this case, the form of the embedding potential and sensitivity of the function $\psi(r)$ to volume changes become the determining factors. If all discrepancies with experiment were attributable to electron contributions to the energy and pressure, they would have to be controlled by laws going beyond the model of the embedded atom.

It should be noted that many studies with the use of EAM investigate systems under isothermal conditions, e.g., at absolute zero. In this case, there are no questions about the effect of temperature. However, questions do arise in connection with phase diagram calculations using the EAM. An encouraging fact is if two phases similar in terms of thermal electron contributions are in equilibrium, the equilibrium persists even in the absence of these contributions. Therefore, the position of lines in the phase diagram changes but insignificantly upon transition from metals to parametals. An example of such a situation is discussed below. However, ignoring the problem of thermal electron contributions can lead to serious errors.

5. Melting temperature in the context of the embedded atom model

Methods for calculating the EAM potential of metals for which static and shock compression data are available were considered in preceding sections. Let us now take into account that the melting point and its dependence on pressure are also important characteristics of the models and make it possible to judge the quality of the interparticle potentials used.

5.1 Determining melting temperature of metal models

It is relatively easy to determine the melting temperature of models by the heating method [7, 8], which measures it in a series of long isothermal runs by recording the mean square of particle displacements $\langle(\Delta r)^2\rangle$ and the maximum value of the structure factor $S(\mathbf{K})$, where $\mathbf{K}$ is the scattering vector:

$$S(\mathbf{K}) = \frac{1}{N}\left|\sum_i \exp\left(-\mathrm{i}\mathbf{K}\mathbf{R}_i\right)\right|^2 . \tag{18}$$

Here, $\mathbf{R}_i$ denotes the coordinates of atoms and N is the number of model particles, in the absence of averaging over all directions. For a single crystal at low temperatures, the maximum values of $S(\mathbf{K}) \sim N$ are achieved in the case of scattering vectors $\mathbf{K}$, which are the vectors of reciprocal lattice nodes. When the model melts, $\langle(\Delta r)^2\rangle$ sharply increases, while $S_{\max}(\mathbf{K})$ decreases abruptly from $\sim N$ to $\sim 20-30$. When determining the melting temperature T_{m}, one can use either the model of an ideal crystal or that of a crystal with a small number of defects (e.g., vacancies). If melting does not occur at a given temperature for 100–200 thousand time steps, then the temperature can be increased by a certain value, etc. The reheating method is quite simple, but subject to the risk of overheating the solid phase by about a few ten degrees Kelvin.

On the other hand, there is a two-phase technique in which the model consists of two layers (crystalline and liquid) with a flat boundary between them and a temperature selected so that both layers are in equilibrium [21]. These methods can be compared based on the results of simulation of lithium melting models with a potential [7, 73, 78]. The two-phase method was used in [21] and the reheating method in [7]. The results are shown in Table 22. The two-phase method produces a relatively small overestimation of T_{m} over real

Table 22. Melting temperature T_m of simulated and real lithium.

Pressure, GPa	T_m, K		
	[21]	[7]	Real Li [27]
0	482	556	454
2.5	570	647	505
4.0	—	634	520

values (by 30–70 K) due to the incomplete adequacy of the potential, while the reheating method overestimates T_m by an additional 60–80 K due to solid phase overheating.

The third method is designed to calculate the temperature (under a given pressure) at which the Gibbs energies of the liquid and solid phases are equal. The following discussion is focused on the results obtained mainly by the simpler reheating method.

To recall, the agreement between the calculated pressures of the models under static conditions and/or at the shock adiabat and the real pressures does not guarantee agreement between calculated and actual melting lines. The calculated melting lines can go both above and below the real ones, as exemplified below. In the case of such discrepancies, a correction of the interparticle potential is required. Therefore, it is necessary to find out what corrections of the EAM potential will lead to the desired change in the shape of the melting line.

5.2 Taking account of electron contributions to the energy and pressure

An analysis can begin with the question of how the calculated melting line is affected taking into account or ignoring electron contributions to the energy and pressure. Table 23 shows results of the calculation of the melting line of aluminum models by the heating method. Variants of proto-aluminum and aluminum with EAM-1, EAM-2, and EAM-3 potentials were investigated, with and without regard for electron contributions to the energy and pressure (see Section 4.3). It can be seen that calculated melting temperatures in these variants are very similar, and only at a pressure of 200 GPa is there a significant difference between them (by no more than 2%). The calculated melting temperatures of aluminum are greatly overestimated compared with experimental data [34].

Table 23. Melting temperature of aluminium models.

Model	Pressure, GPa				
	0	50	100	150	200
	Melting temperature, K (±5 K)				
Proto-Al	790	3943	4944	—	—
EAM-1	1132	3734	5093	5982	6792
EAM-2	1132	3918	5062	5965	6665
EAM-3	1132	3806	5106	—	—
[92]	930	—	—	—	—
[119]	—	3100	4000	—	—
Experiment [34]	933.4	2910	—	—	—

Similarly to the case of aluminum, it is possible to calculate pressure dependences of melting temperature T_m of nickel models taking into account (EAM-B) or ignoring (para-nickel, EAM-A) electron contributions to the energy. The results for fcc and bcc lattice melting are presented in Table 24. A comparison of melting temperatures of various nickel structures with different potentials shows that (1) the fcc lattice at the melting line is more stable than the bcc lattice at pressures below 120 GPa (when its melting temperature is higher) and less stable at higher pressures, (2) the difference between melting temperatures for EAM-A and EAM-B potentials is not very large and does not exceed 50–80 K even at pressures $\sim$ 600 GPa, i.e., about 1.5%, (3) a triple point (fcc–bcc–fluid) must exist at the melting line near 120 GPa, (4) a bcc phase region must exist on the phase diagram of Ni models with EAM-A, B potentials at pressures above 120 GPa.

Real nickel melting temperatures are subject to marked variation. According to [36], T_m values in [121–123] are underestimated for technical reasons. Taking this estimate for granted while being guided by the experimental data in [36] leads to the conclusion that calculations with EAM potentials underestimate the melting point of nickel by 300–600 K.

Finally, let us consider the behavior of the tin melting line based on the data obtained in diamond cells under pressures up to 30–68 GPa [124–126], up to 105 GPa [127], and up to

Table 24. Pressure dependence of para-nickel and nickel model melting temperatures.

Object, reference	Method	Pressure, GPa										
		0	25	50	100	150	200	250	300	400	500	600
		Melting temperature, K										
bcc	EAM-A	1437	—	2544	3231	3706	4056	4356	4518	4843	5118	5332
bcc	EAM-B	1437	—	2544	3231	3706	4090	4332	4518	4806	5040	5281
fcc	EAM-A	1656	2332	2733	3283	3668	4018	4281	4456	—	—	—
fcc	EAM-B	1656	2332	2733	3283	3668	4031	4318	4456	—	—	—
fcc	EAM-D	1656	—	—	3356	3878	4394	–	5294	—	—	—
[110]	Analytical	1728	—	2870	3760	4290	4810	5190	5510	—	—	—
[120]	*Ab initio*	1750	2440	3000	—	—	—	—	—	—	—	—
[36]	Static	—	2635	3000	3690	4280	—	—	—	—	—	—
[121 – 123]	Static	—	2200	2400	—	—	—	—	—	—	—	—

Table 25. Pressure dependence of fcc tin model melting temperature.

System	Potential	Model pressure, GPa							
		7.5	10.0	20	32.2	44.8	57.3	75	125
		Model temperature, K							
Proto-Sn	Pair contribution	1623	—	—	—	—	6100	—	9910
Para-Sn	EAM-A	741	894	1468	2268	—	4088	5506	8556
Sn	EAM-B	741	894	1468	2268	—	4088	5375	8268
Experiment [127]	—	—	1150	1620	1920	2200	2430	—	—

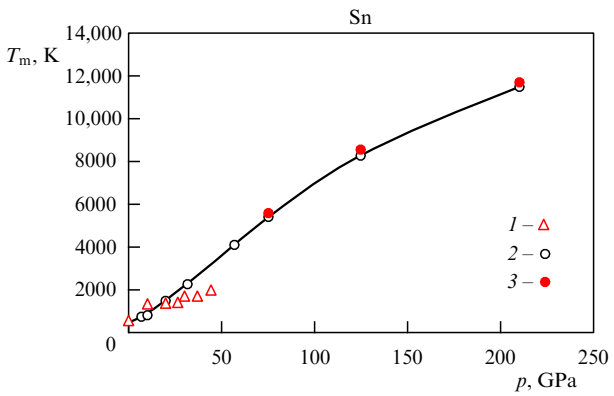

Figure 21. Melting temperatures. *1* — real tin, *2* — Sn models taking into account electron contributions, *3* — para-tin models disregarding electron contributions.

40 GPa by the *ab initio* method [118]. Melting temperatures of tin models were calculated by the reheating method [7]. T_m values of proto-tin, para-tin, and tin are presented in Fig. 21 and Table 25. The calculated T_m values are inconsistent with experimental ones [127]. However, the difference between T_m values in models with EAM-A and EAM-B potentials does not exceed 3.4%.

Table 25 also shows the melting point of the proto-tin models built taking into account only pair contribution to the EAM potential. It gradually approaches (from above) the T_m values for para-tin and tin models as pressure grows due to the increasing role of the repulsive forces in metal compression and atom convergence controlled by the repulsive branch of the pair contribution to the potential.

In all the cases considered, the melting point depends little on the consideration or disregard of electron contributions, the cause being that the Gibbs energies of the two phases are equal at their equilibrium point and for the corresponding parametals if their electron contributions to the energy and pressure are comparable. This is an encouraging fact, especially for molecular dynamics calculations of the melting line, since it makes possible a rough determination of the melting line without considering electron contributions, the magnitude of which is often unknown.

5.3 Correction of the shape of the melting line of metal models

When applying the method for calculating the EAM potential described in [7], the pair contribution to the potential is determined from the form of the pair correlation function of the fluid slightly above the melting point (the Schommers algorithm), and the embedding potential is found from the shape of the SA or from static compression

Table 26. Lead model melting temperature.

Model	Pressure, GPa				
	0	25	50	75	100
	Melting temperature, K				
[21, 128]	—	1880	2490	3030	3450
[130]	—	2100	3200	4000 [c]	?
[129]	—	1830	2770	3510	4180 [c]
Proto-Pb	662	—	3583	—	4981
Proto-1 [a]	662	—	4332	—	6893
Proto-2 [b]	662	—	2768	—	2994
EAM-1 [7, 112]	531	1967	2834	3381	3805
EAM-2	—	1943	2866	3483	4006

[a] Steepness of the repulsive branch is magnified, [b] steepness is diminished, [c] extrapolation.

data. It would seem that there are no degrees of freedom left to refine the EAM potential taking into account the shape of the melting line. However, this is not so. The pair contribution to the potential is determined by the Schommers algorithm only for distances r exceeding the minimum interparticle distance r_{min} in the fluid near the melting point, while the form of the embedding potential at $r < r_{min}$ remains unknown and should be chosen additionally.

So, it is necessary to find out to what extent the form of the EAM potential at $r < r_{min}$ is sensitive so as to calculate the melting temperature of the model. The easiest way to check this is through an example of a protometal without regard for the embedding potential. To this effect, melting points of proto-lead models were calculated differing in the steepness of the repulsive branches of the pair contribution to the EAM potential. Table 26 shows lead melting temperatures measured by static [31, 128, 129] and shock [130] compression methods, as well as the MD method, taking into account electron contributions [7, 131] (hereinafter EAM-1) and with the EAM-1 potential without regard for the embedding potential, i.e., for proto-lead (proto-Pb, proto-1, proto-2). The pair contribution to the EAM-1 potential [7, 131] at $r < 2.60$ Å has the form

$$\varphi(r)\,[\mathrm{eV}] = 0.438472 + (1.49474 - 5.488)(2.60 - r) + 2.8\{\exp[1.96(2.60 - r)] - 1\}\,. \quad (19)$$

It is this pair potential at the distance $r < 2.60$ Å that is used to construct the proto-Pb model. The potential steepness is

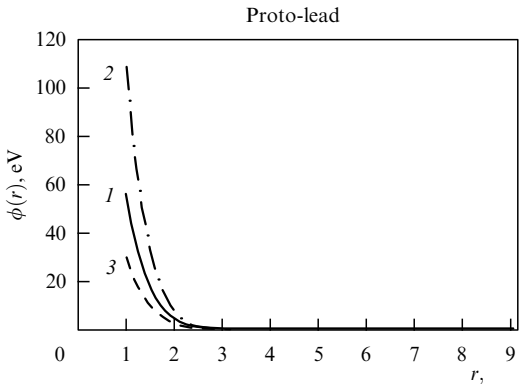

Figure 22. Pair contributions to the proto-lead potential. *1* — formula (19), *2* — (20), *3* — (21).

increased in the case of the proto-1 model:

$$\varphi_1(r)\left[\mathrm{eV}\right] = 0.438472 + (1.49474 - 2\times 5.488)(2.60 - r) + 2.8\times 2\left\{\exp\left[1.96(2.60 - r)\right] - 1\right\}, \qquad (20)$$

and diminished in the case of the proto-2 model:

$$\varphi_2(r)\left[\mathrm{eV}\right] = 0.438472 + \left(1.49474 - \frac{5.488}{2}\right)(2.60 - r) + \frac{2.8}{2}\left\{\exp\left[1.96(2.60 - r)\right] - 1\right\}. \qquad (21)$$

Three variants of pair contributions to the lead potential are shown in Fig. 22. It can be seen from Table 26 that the melting temperature of the models increases as the steepness of the pair contribution to the potential at small distances goes up, and decreases with decreasing steepness, while the sensitivity of the melting temperature to the steepness is rather high. This suggests that the choice of a proper steepness of the pair contribution to the potential at $r < r_{\min}$ may be instrumental in the improvement of the agreement between melting temperature of models and the real melting line.

Taking into account the data from Table 26, it is possible to improve the agreement between theoretical and measured lead melting points [129] by increasing the steepness of the repulsive branch of the pair contribution to the potential. Table 26 shows melting temperatures of the lead model with a pair contribution at $r < 2.60$ Å in the form

$$\varphi(r)\left[\mathrm{eV}\right] = 0.438472 - 4.83326(2.60 - r) + 2.8\left\{\exp\left[2.26(2.60 - r)\right] - 1\right\} \qquad (22)$$

(EAM-2 potential), where the coefficient in the exponent is increased from 1.96 to 2.26. It follows from Table 26 that the EAM-2 potential leads to much better agreement with experiment [129]. Variation of the repulsive branch allows significantly improving the agreement with the real melting line.

Note that the transition from expression (19) to (22) has very little effect on the properties of lead models. At a density of 18.768 g cm^{-3} and a temperature of 4012 K, the pressure of liquid lead increases from 98.75 to 99.95 GPa, and the energy decreases from 106.21 to 104.79 kJ mol^{-1}.

Similar calculations were made for nickel models. The steepness of the repulsive branch of the pair contribution to the EAM-B potential (Morse potential [109]) was increased by adding to the potential the expression $\Delta\varphi(r) = a_{\mathrm{d}}(1.85 - r)^2 H(1.85 - r)$, where $H(t)$ is the Heaviside function and r is expressed in Å. Let us denote the potential with this addition by EAM-D. T_{m} values obtained at $a_{\mathrm{d}} = 45.0$ eV Å^{-2} are presented in Table 24. The addition of $\Delta\varphi(r)$ increases the melting temperature in nickel models by 70–800 K to a value close to the analytically calculated one [110].

To sum up, of primary importance in the context of the embedded atom model is the choice of the repulsive branch of the potential at distances $r < r_{\min}$ to which the melting temperature of the model is sensitive. The *ab initio* method making it possible to estimate the interparticle interaction forces at distances much less than $r_{\min}$ can greatly facilitate the choice. Therefore, the use of the *ab initio* method to find the functions setting the EAM potential can be very effective.

6. Conclusion

Returning to the discussion of metal and parametal models and their parameters considered above, it should be emphasized that taking into account/disregarding thermal electron contributions to the energy and pressure can strongly affect the results of calculations at high pressures and temperatures. Therefore, the verification of the EAM potential requires that its predictive power be estimated and agreement with experiment evaluated at either 0 or 298 K and under shock compression conditions (i.e., for a tandem). At the same time, the melting lines calculated with and without regard for thermal electron contributions turn out to be very close, rarely differing in excess of 100 K. This situation is very favorable for the calculation of melting lines (and indeed every two-phase equilibrium line), since, in this case, it is possible to ignore electron contributions, about which little is known in most cases. A good result was obtained by this method, e.g., for iron [95]. For this purpose, it is sufficient to calculate the EAM potential for a parametal from shock compression data, which is much easier to do than by taking into consideration thermal electron contributions. This approach is often used to calculate the state of a planetary core.

The similarity of melting temperatures in metal and parametal models at the same pressure is ensured by the similarity of the amplitudes of interparticle forces arising from local lattice distortions, leading to melting. Forces with the same amplitudes control the self-diffusion process in a fluid. Therefore, it is interesting to compare the self-diffusion coefficients in the models of liquid metals and parametals at the same pressure or the same density. Table 27 shows calculated self-diffusion coefficients for Al, Sn, Bi, Ni, and their para-twins at the same temperatures and densities/pressures. Indeed, self-diffusion coefficients in metal and parametal models at the same temperatures and densities agree very well. Thus, the self-diffusion coefficients can be estimated using parametal models in the absence of information on thermal electron contributions. This possibility is most useful for calculating the properties of transition metals in which electron contributions are especially large.

Bearing in mind the well-known Stokes–Einstein relation between coefficients of self-diffusion D and viscosity η, $D = kT/(4\pi\eta r_{\mathrm{a}})$ (r_{a} is the effective radius of an atom), it can be concluded that the similarity of self-diffusion coefficients in metal and parametal models accounts for the closeness of

Table 27. Self-diffusion coefficients in metal models.

Model	Density, g cm^{-3}	Pressure, GPa	T, K	$D \times 10^5$, cm^2 s^{-1}
Al	4.86	205.2	7000	11.92
Para-Al	4.86	197.0	7000	11.86
Para-Al	4.93	205.2	7000	11.76
Sn	12.33	125.0	8500	9.57
Para-Sn	12.33	119.7	8500	10.49
Para-Sn	12.51	124.9	8500	8.64
Bi	15.77	50.19	3000	6.39
Para-Bi	15.77	47.64	3000	6.05
Para-Bi	16.10	50.22	3000	5.72
Ni	15.14	500	5200	6.97
Para-Ni	15.14	465	5200	6.90
Para-Ni	15.37	500	5200	7.07

their shear viscosities. This fact is also beneficial for MD calculations of the properties of liquid metals.

References

1. Daw M S, Baskes M I *Phys. Rev. B* **29** 6443 (1984)
2. Finnis M W, Sinclair J E *Philos. Mag. A* **50** 45 (1984)
3. Foiles S M, Baskes M I, Daw M S *Phys. Rev. B* **33** 7983 (1986)
4. Voter A F, Chen S P *MRS Proc.* **82** 175 (1986)
5. Sutton A P, Chen J *Philos. Mag. Lett.* **61** 139 (1990)
6. Norman G E, Stegailov V V *Math. Models Comput. Simul.* **5** 305 (2013); *Matem. Modelirovanie* **24** (6) 3 (2012)
7. Belashchenko D K *Liquid Metals: From Atomistic Potentials to Properties, Shock Compression, Earth s Core and Nanoclusters* (New York: Nova Science Publ., 2018)
8. Belashchenko D K *Phys. Usp.* **56** 1176 (2013); *Usp. Fiz. Nauk* **183** 1281 (2013)
9. Schommers W *Phys. Lett. A* **43** 157 (1973)
10. Reatto L *Philos. Mag. A* **58** 37 (1988)
11. Munejiri Sh et al. *J. Non-Cryst. Solids* **205–207** 278 (1996)
12. Belashchenko D K, Gelchinski B R *J. Non-Cryst. Solids* **353** 3515 (2007)
13. Pozzo M, Alfè D *Phys. Rev. B* **88** 024111 (2013)
14. Cao Q-L et al. *J. Chem. Phys.* **140** 114505 (2014)
15. Cao Q-L et al. *Chinese Phys. Lett.* **32** 086201 (2015)
16. Banerjea A, Smith J R *Phys. Rev. B* **37** 6632 (1988)
17. Cai J, Ye Y Y *Phys. Rev. B* **54** 8398 (1996)
18. Baskes M I *Phys. Rev. B* **46** 2727 (1992)
19. Lee B J et al. *Phys. Rev. B* **64** 184102 (2001)
20. Doyama M, Kogure Y *Comput. Mater. Sci.* **14** 80 (1999)
21. Vella J R et al. *J. Phys. Chem. B* **119** 8960 (2015)
22. Vinet P et al. *J. Geophys. Res.* **92** 9319 (1987)
23. Dewaele A et al. *Phys. Rev. B* **78** 104102 (2008)
24. Shock Wave Database, http://www.ihed.ras.ru/rusbank/
25. Marsh S P (Ed.) *LASL Shock Hugoniot Data* (Berkeley, CA: Univ. of California Press, 1980)
26. Al'tshuler L V et al. *J. Appl. Mech. Tech. Phys.* **22** 145 (1981); *Zh. Priklad. Mekh. Tekh. Fiz.* (2) 3 (1981)
27. Guillaume Ch L et al. *Nat. Phys.* **7** 211 (2011)
28. Gregoryanz E et al. *Science* **320** 1054 (2008)
29. Narygina O et al. *Phys. Rev. B* **84** 054111 (2011)
30. Boehler R, Zha C *Physica B + C* **139–140** 233 (1986)
31. Tonkov E Yu, Ponyatovsky E G *Phase Transformations of Elements under High Pressure* (Boca Raton, FL: CRC Press, 2005)
32. Jayaraman A, Newton R C, McDonough J M *Phys. Rev.* **159** 527 (1967)
33. Boehler R, Ross M *Earth Planet. Sci. Lett.* **153** 223 (1997)
34. Hänström A, Lazor P *J. Alloys Compd.* **305** 209 (2000)
35. Hemley R J, Mao H-K *Int. Geology Rev.* **43** 1 (2001)
36. Lord O T et al. *Earth Planet. Sci. Lett.* **408** 226 (2014)
37. Landau L D, Lifshitz E M *Fluid Mechanics* (London: Pergamon Press, 1959); Translated from Russian: *Mekhanika Sploshnykh Sred* (Moscow: Gostekhteorizdat, 1954)
38. Zel'dovich Ya B, Raizer Yu P *Physics of Shock Waves and High-Temperature Hydrodynamic Phenomena* (New York: Academic Press, 1966, 1967); Translated from Russian: *Fizika Udarnykh Voln i Vysokotemperaturnykh Gidrodinamicheskikh Yavlenii* (Moscow: Nauka, 1966)
39. McQueen R G, Marsh S P *J. Appl. Phys.* **31** 1253 (1960)
40. Al'tshuler L V, Bakanova A A, Trunin R F *Sov. Phys. JETP* **15** 65 (1962); *Zh. Eksp. Teor. Fiz.* **42** 91 (1962)
41. Walsh J M et al. *Phys. Rev.* **108** 196 (1957)
42. Al'tshuler L V et al. *Sov. Phys. JETP* **7** 874 (1958); *Zh. Eksp. Teor. Fiz.* **34** 874 (1958)
43. Al'tshuler L V et al. *Sov. Phys. JETP* **11** 766 (1960); *Zh. Eksp. Teor. Fiz.* **38** 1061 (1960)
44. Al'tshuler L V, Chekin B S, in *Doklady I Vsesoyuz. Simpoziuma po Impul'snym Davleniyam, Moscow, 24–26 Oktyabrya 1973 g.* (Proc. of the 1st All-Union Symp. on Impulse Pressures, Moscow, October 24–26, 1973) Vol. 1 (Moscow: VNIIFTRI, 1974) p. 5
45. Brown J M, Fritz J N, Hixson R S *J. Appl. Phys.* **88** 5496 (2000)
46. Trunin R F et al. *Eksperimental'nye Dannye po Udarno-volnovomy Szhatiyu i Adiabaticheskomu Rasshireniyu Kondensirovannykh Veshchestv* (Experimental Data on Shock-Wave Compression and Adiabatic Expansion of Condensed Matter) (Ed. R F Trunin) (Sarov: RFYaTs—VNIIEF, 2001)
47. Zharkov V N, Kalinin V A *Equations of State for Solids at High Pressures and Temperatures* (New York: Consultants Bureau, 1971); Translated from Russian: *Uravneniya Sostoyaniya Tverdykh Tel pri Vysokikh Davleniyakh i Temperaturakh* (Moscow: Nauka, 1968)
48. Trunin R F et al. *J. Exp. Theor. Phys.* **76** 1095 (1993); *Zh. Eksp. Teor. Fiz.* **103** 2189 (1993)
49. Medvedev A B, Trunin R F *Phys. Usp.* **55** 773 (2012); *Usp. Fiz. Nauk* **182** 829 (2012)
50. Kormer S B et al. *Sov. Phys. JETP* **15** 477 (1962); *Zh. Eksp. Teor. Fiz.* **42** 686 (1962)
51. Slater J C *Introduction to Chemical Physics* (New York: Dover Publ., 1939)
52. Landau L D, Stanyukovich K P *Dokl. Akad. Nauk SSSR* **46** 399 (1945)
53. Boness D A, Brown J M, McMahan A K *Phys. Earth Planet. Inter.* **42** 227 (1986)
54. Wasserman E, Stixrude L, Cohen R E *Phys. Rev. B* **53** 8296 (1996)
55. Belonoshko A B, Ahuja R, Johansson B *Phys. Rev. Lett.* **84** 3638 (2000)
56. Lin Z, Zhigilei L V, Celli V *Phys. Rev. B* **77** 075133 (2008)
57. Lin Z, Zhigilei L V *Appl. Surf. Sci.* **253** 6295 (2007)
58. Electron-Phonon Coupling and Electron Heat Capacity in Metals at High Electron Temperatures, http://www.faculty.virginia.edu/CompMat/electron-phonon-coupling/
59. Bévillon E et al. *Phys. Rev. B* **89** 115117 (2014)
60. Belashchenko D K *Russ. J. Phys. Chem. A* **87** 615 (2013); *Zh. Fiz. Khim.* **87** 633 (2013)
61. Landau L D, Lifshitz E M *Statistical Physics* (London: Pergamon Press, 1958); Translated from Russian: *Statisticheskaya Fizika* (Moscow: GITTL, 1951)
62. Al'tshuler L V et al. *Sov. Phys. JETP* **51** 373 (1980); *Zh. Eksp. Teor. Fiz.* **78** 741 (1980)
63. Levashov P R et al. *J. Phys. Condens. Matter* **22** 505501 (2010)
64. Migdal K P, Thesis for Cand. Phys.-Math. Sci. (Moscow: BNIIA bv. N L Dukhova, 2017)
65. Louis A A *J. Phys. Condens. Matter* **14** 9187 (2002)
66. Brommer P, Gähler F *Modelling Simul. Mater. Sci. Eng.* **15** 295 (2007)
67. Mendelev M I et al. *Philos. Mag.* **92** 4454 (2012)
68. Mendelev M I et al. *Philos. Mag.* **83** 3977 (2003)
69. Alfè D, Price G D, Gillan M J *Phys. Rev. B* **65** 165118 (2002)
70. Belashchenko D K, Smirnova D E *Russ. J. Phys. Chem. A* **85** 1908 (2011); *Zh. Fiz. Khim.* **85** 2048 (2011)
71. Waseda Y *The Structure of Non-Crystalline Materials. Liquids and Amorphous Solids* (New York: McGraw-Hill, 1980)

72. Bakanova A A, Dudoladov I P, Trunin R F *Sov. Phys. Solid State* **7** 1307 (1965); *Fiz. Tverd. Tela* **7** 1615 (1965)
73. Belashchenko D K *High Temp.* **51** 626 (2013); *Teplofiz. Vys. Temp.* **51** 697 (2013)
74. Bystrov P I et al. *Liquid-Metal Coolants for Heat Pipes and Power Plants* (Ed. V A Kirillin) (New York: Hemisphere Publ. Corp., 1990); Translated from Russian: *Zhidkometallicheskie Teplonositeli Teplovykh Trub i Energeticheskikh Ustanovok* (Exec. Ed. V A Kirillin) (Moscow: Nauka, 1988)
75. Winzenick M, Vidjayakumar V, Holzapfel W B *Phys. Rev. B* **50** 12381 (1994)
76. McBride E E "On structural studies of high-density potassium and sodium", Thesis (Edinburgh: Univ. of Edinburgh, 2013) submitted in fulfilment of the requirements for the degree of Doctor of Philosophy
77. Young D A, Ross M *Phys. Rev. B* **29** 682 (1984)
78. Belashchenko D K *High Temp.* **50** 331 (2012); *Teplofiz. Vys. Temp.* **50** 354 (2012)
79. Rice M H *J. Phys. Chem. Solids* **26** 483 (1965)
80. Grover R et al. *J. Phys. Chem. Solids* **30** 2091 (1969)
81. Al'tshuler L V et al. *Sov. Phys. JETP* **11** 573 (1960); *Zh. Eksp. Teor. Fiz.* **38** 790 (1960)
82. Glushak B L et al. *Sov. Phys. JETP* **69** 739 (1989); *Zh. Eksp. Teor. Fiz.* **96** 1301 (1989)
83. Garai J, Chen J, Telekes G *Calphad* **33** 737 (2009)
84. Dewaele A, Loubeyre P, Mezouar M *Phys. Rev. B* **70** 094112 (2004)
85. Belashchenko D K, Vorotyagin A V, Gelchinsky B R *High Temp.* **49** 656 (2011); *Teplofiz. Vys. Temp.* **49** 676 (2011)
86. Oh D J, Johnson R A *J. Mater. Res.* **3** 471 (1988)
87. Rohrer C L *Modelling Simul. Mater. Sci. Eng.* **2** 119 (1994)
88. Mishin Y et al. *Phys. Rev. B* **59** 3393 (1999)
89. Morozov I V et al. *Comput. Phys. Commun.* **182** 1974 (2011)
90. Ercolessi F, Adams J B *Europhys. Lett.* **26** 583 (1994)
91. Mendelev M I et al. *Philos. Mag.* **88** 1723 (2008)
92. Liu X-Y, Ercolessi F, Adams J B *Modelling Simul. Mater. Sci. Eng.* **12** 665 (2004)
93. McQueen R G et al., in *High-Velocity Impact Phenomena* (Ed. R Kinslow) (New York: Academic Press, 1970) p. 293; "Appendix A — shock wave data for standard materials", in *High Velocity Impact Phenomena* (Ed. R Kinslow) (New York: Academic Press, 1970) appendices on p. 515
94. Dewaele A et al. *Phys. Rev. Lett.* **97** 215504 (2006)
95. Belashchenko D K, Ostrovskii O I *Russ. J. Phys. Chem. A* **85** 967 (2011); *Zh. Fiz. Khim.* **85** 1063 (2011)
96. Dorogokupets P I et al. *Sci. Rep.* **7** 41863 (2017)
97. Hixson R S, Winkler M A, Hodgdon M L *Phys. Rev. B* **42** 6485 (1990)
98. Assael M J et al. *J. Phys. Chem. Ref. Data* **35** 285 (2006)
99. Belashchenko D K, Magidson I A *Izv. Vyssh. Ucheb. Zaved. Chernaya Metallurg.* (3) 4 (1983)
100. Mendelev M I, Belashchenko D K *Metally* (3) 21 (1995)
101. Landa A et al. *Acta Mater.* **46** 3027 (1998)
102. Vitek V, Ackland G J, Cserti J *MRS Proc.* **186** 237 (1990)
103. Baskes M I *Mater. Chem. Phys.* **50** 152 (1997)
104. Zhang Q, Lai W S, Liu B X *J. Non-Cryst. Solids* **261** 137 (2000)
105. Koči L et al. *Phys. Rev. B* **74** 012101 (2006)
106. Özgen S, Sonğur L, Kara İ *Turk. J. Phys.* **36** 59 (2012)
107. Cherne F J, Baskes M I, Deymier P A *Phys. Rev. B* **65** 024209 (2001)
108. Alemany M M G et al. *J. Non-Cryst. Solids* **250–252** 53 (1999)
109. Belashchenko D K *High Temp.* **58** 64 (2020); *Teplofiz. Vys. Temp.* **58** 61 (2020)
110. Urlin V D *Sov. Phys. JETP* **22** 341 (1966); *Zh. Eksp. Teor. Fiz.* **49** 485 (1965)
111. Salamat A et al. *Phys. Rev. B* **84** 140104(R) (2011)
112. Gavriliuk A G et al. *JETP Lett.* **106** 733 (2017); *Pis'ma Zh. Eksp. Teor. Fiz.* **106** 702 (2017)
113. Belashchenko D K *Russ. J. Phys. Chem.* **75** 81 (2001); *Zh. Fiz. Khim.* **75** 89 (2001)
114. Belashchenko D K *High Temp.* **59** (2021) in press; *Teplofiz. Vys. Temp.* **59** (2021) in press
115. Itami T et al. *Phys. Rev. B* **67** 064201 (2003)
116. Munejiri S et al. *J. Phys. Conf. Ser.* **98** 042010 (2008)
117. del Rio B G, González L E *EPJ Web Conf.* **151** 03003 (2017)
118. Bernard S, Maillet J B *Phys. Rev. B* **66** 012103 (2002)
119. Gubin S A et al. *Phys. Procedia* **72** 338 (2015)
120. Minakov D V, Levashov P R *Phys. Rev. B* **92** 224102 (2015)
121. Japel S et al. *Phys. Rev. Lett.* **95** 167801 (2005)
122. Errandonea D *Phys. Rev. B* **87** 054108 (2013)
123. Lazor P, Shen G, Saxena S K *Phys. Chem. Minerals* **20** 86 (1993)
124. Weir S T et al., LLNL-JRNL-522418 (Livermore, CA: Lawrence Livermore National Laboratory, 2012)
125. La Lone B M et al. *J. Appl. Phys.* **126** 225103 (2019)
126. Schwager B et al. *J. Chem. Phys.* **133** 084501 (2010)
127. Briggs R et al. *Phys. Rev. B* **95** 054102 (2017)
128. Godwall B K et al. *Science* **248** 462 (1990)
129. Dewaele A et al. *Phys. Rev. B* **73** 144106 (2007)
130. Partouche-Sebban D et al. *J. Appl. Phys.* **97** 043521 (2005)
131. Belashchenko D K *High. Temp.* **55** 370 (2017); *Teplofiz. Vys. Temp.* **55** 386 (2017)